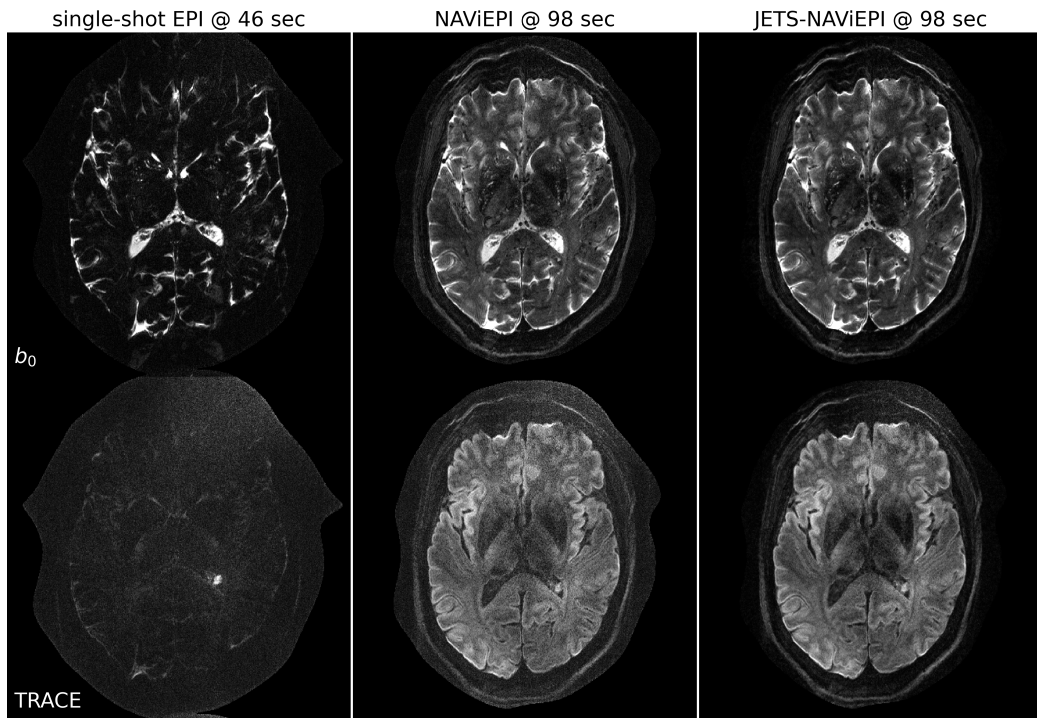


## Graphical Abstract

### Accelerated Diffusion Weighted Magnetic Resonance Imaging at 7 T: Joint Reconstruction for Shift-Encoded Navigator-based Interleaved Echo Planar Imaging (JETS-NAViEPI)

Zhengguo Tan, Patrick Alexander Liebig, Robin Martin Heidemann, Frederik Bernd Laun, Florian Knoll

**3-scan trace acquisition with voxel size 0.5 X 0.5 X 2.0 mm<sup>3</sup>**



## Highlights

### **Accelerated Diffusion Weighted Magnetic Resonance Imaging at 7 T: Joint Reconstruction for Shift-Encoded Navigator-based Interleaved Echo Planar Imaging (JETS-NAViEPI)**

Zhengguo Tan, Patrick Alexander Liebig, Robin Martin Heidemann, Frederik Bernd Laun, Florian Knoll

- Navigator-based interleaved EPI acquisition with minimal distortion mismatch between echoes
- Novel accelerated diffusion acquisition with shifted phase encoding among diffusion directions for complementary  $k$ - $q$ -space sampling at 7 T
- Generalized joint  $k$ - $q$ -slice diffusion-weighted image reconstruction with overlapping locally low-rank regularization
- Efficient simultaneous multi-slice (SMS) image reconstruction
- 3-scan trace acquisition with the voxel size  $0.5 \times 0.5 \times 2.0 \text{ mm}^3$  and 60 slices at 1.5 min

# Accelerated Diffusion Weighted Magnetic Resonance Imaging at 7 T: Joint Reconstruction for Shift-Encoded Navigator-based Interleaved Echo Planar Imaging (JETS-NAViEPI)

Zhengguo Tan<sup>a</sup>, Patrick Alexander Liebig<sup>b</sup>, Robin Martin Heidemann<sup>b</sup>,  
Frederik Bernd Laun<sup>c</sup>, Florian Knoll<sup>a</sup>

<sup>a</sup>*Department Artificial Intelligence in Biomedical Engineering (AIBE),  
Friedrich-Alexander University of Erlangen-Nuremberg, Erlangen, Germany*

<sup>b</sup>*Siemens Healthcare GmbH, Erlangen, Germany*

<sup>c</sup>*Institute of Radiology, University Hospital Erlangen, Friedrich-Alexander University of Erlangen-Nuremberg, Erlangen, Germany*

---

## Abstract

The pursuit of high spatial-angular-temporal resolution for in vivo diffusion-weighted magnetic resonance imaging (DW-MRI) at ultra-high field strength (7 T and above) is important in understanding brain microstructure and function. Such pursuit, however, faces several technical challenges. First, increased off-resonance and shorter  $T_2$  relaxation require faster echo train readouts. Second, existing high-resolution DW-MRI techniques usually employ in-plane fully-sampled multi-shot EPI, which not only prolongs the scan time but also induces a high specific absorption rate (SAR) at 7 T. To address these challenges, we develop in this work navigator-based interleaved EPI (NAViEPI) which enforces the same effective echo spacing (ESP) between the imaging and the navigator echo. First, NAViEPI renders no distortion mismatch between the two echoes, and thus simplifies shot-to-shot phase variation correction. Second, NAViEPI allows for a large number of shots

(e.g. > 4) with undersampled iEPI acquisition, thereby rendering clinically-feasible high-resolution sub-millimeter protocols. To retain signal-to-noise ratio (SNR) and to reduce undersampling artifacts, we developed a  $k_y$ -shift encoding among diffusion encodings to explore complementary  $k$ - $q$ -space sampling. Moreover, we developed a novel joint reconstruction with overlapping locally low-rank regularization generalized to the multi-band multi-shot acquisition at 7 T (dubbed JETS-NAViEPI). Our method was demonstrated with experimental results covering 1 mm isotropic resolution multi  $b$ -value DWI and sub-millimeter in-plane resolution fast TRACE acquisition.

*Keywords:* Diffusion-weighted magnetic resonance imaging, Echo planar imaging, Navigator, Ultra-high field, Joint reconstruction, Low rank, Simultaneous multi slice

---

<sup>1</sup> **1. Introduction**

<sup>2</sup> Diffusion-weighted magnetic resonance imaging (DW-MRI) ([Le Bihan et al., 1986; Merboldt et al., 1985](#)) is a non-invasive modality that is sensi-  
<sup>3</sup> tive to the intravoxel Brownian motion of water molecules. DW-MRI forms  
<sup>4</sup> the basis for diffusion tensor imaging (DTI) ([Basser et al., 1994; Mori et al., 1999](#)) and high angular resolution diffusion imaging (HARDI) ([Tuch et al., 2002](#)), and has been widely used in acute brain ischemia diagnosis, in tumor  
<sup>5</sup> detection and staging, and in neuroscience ([Jones, 2010](#)).

<sup>6</sup> For DW-MRI acquisition, the commonly used pulse sequence is single-  
<sup>7</sup> shot echo-planar imaging (SS-EPI) ([Mansfield, 1977](#)). SS-EPI is capable of  
<sup>8</sup> rapidly acquiring one DW image per radio-frequency excitation at the order  
<sup>9</sup> of 100 ms, and is thus motion robust. However, conventional SS-EPI, even  
<sup>10</sup> with three-fold accelerated acquisition ([Bammer et al., 2001](#)) using parallel  
<sup>11</sup> imaging ([Roemer et al., 1990; Ra and Rim, 1993; Pruessmann et al., 1999](#);  
<sup>12</sup> [Griswold et al., 2002](#)), still suffers from low spatial resolution and geometric  
<sup>13</sup> distortions.

<sup>14</sup> In the quest for high spatial-angular-temporal-resolution and minimal-  
<sup>15</sup> geometry-distortion DW-MRI, tremendous efforts have been made. Tech-  
<sup>16</sup> niques for the correction of image distortions induced by off-resonances and  
<sup>17</sup> eddy currents have been developed ([Andersson et al., 2003](#)). Furthermore,  
<sup>18</sup> gSlider ([Setsompop et al., 2018](#)) with blipped-CAIPI ([Setsompop et al., 2012](#))  
<sup>19</sup> for simultaneous multi-slice (SMS) ([Maudsley, 1980; Breuer et al., 2005](#))  
<sup>20</sup> was proposed to achieve high-resolution DW-MRI. Advanced pulse sequences  
<sup>21</sup> based on multi-shot EPI have also been developed, including but not limited  
<sup>22</sup> to interleaved EPI (iEPI) ([Butts et al., 1993](#)), PROPELLER ([Pipe et al., 2004](#)),

26 2002), and readout-segmented EPI (rsEPI) (Porter and Heidemann, 2009;  
27 Heidemann et al., 2010).

28 Based on four-shot iEPI, multiplexed sensitivity encoding (MUSE) image  
29 reconstruction achieved DW-MRI with a sub-millimeter in-plane resolution  
30 and maximal  $b$ -value  $800 \text{ s/mm}^2$  at 3 T (Chen et al., 2013). The four-shot  
31 iEPI employed in MUSE acquired an in-plane fully-sampled  $k$ -space, except  
32 partial Fourier. Every shot (segment), corresponding to four-fold under-  
33 sampling, was then reconstructed via parallel imaging to obtain shot-to-shot  
34 phase variation. This indicates that increasing the number of shots in MUSE  
35 will result in higher undersampling per shot, and consequently, degrade shot  
36 phase estimation (Wu and Miller, 2017).

37 Alternatively, navigator-based iEPI acquisition has been proposed (Jeong  
38 et al., 2013; Dai et al., 2017, 2018). These proposals allow for a larger num-  
39 ber of shots, and hence higher spatial resolution. However, due to the use of  
40 different ESP between the imaging echo and the navigator echo, these pro-  
41 posals suffered from geometric distortion mismatch between the two echoes  
42 and thus required specific compensation methods. In contrast, rsEPI (Porter  
43 and Heidemann, 2009; Heidemann et al., 2010) used the same readout seg-  
44 ment for both echoes, and thus required no distortion correction of navigator  
45 echoes.

46 Beyond the MUSE-type parallel imaging reconstruction, compressed sens-  
47 ing (Lustig et al., 2007; Block et al., 2007) has been explored. For instance,  
48 multi-shot reconstruction techniques based on structured low-rank matrix  
49 completion (MUSSELS) (Mani et al., 2017; Bilgic et al., 2019) achieved 5-  
50 shot DW-MRI with 9-fold undersampling per shot. Recently, JULEP (Dai

51 et al., 2023) incorporated explicit phase mapping into MUSSELS. These re-  
52 construction techniques, i.e., MUSE, MUSSELS and JULEP, targeted the  
53 reconstruction of one DW image from interleaved EPI acquisition, and did  
54 not explore joint- $k$ - $q$ -space undersampling or reconstruction.

55 Joint- $k$ - $q$ -space undersampling can be achieved via proper regularization  
56 along the diffusion encoding direction. Relevant examples are diffusion un-  
57 dersampling with Gaussian process estimated reconstruction (DAGER) (Wu  
58 et al., 2019) and magnitude-based spatial-angular locally low-rank regular-  
59 ization (SPA-LLR) (Hu et al., 2020). However, DAGER addressed the re-  
60 construction problem of single-shot EPI acquisition and SPA-LLR focused  
61 on the reconstruction of single-band and fully-sampled iEPI acquisition.

62 In this work, we propose a Joint  $k$ - $q$ -slice rEconsTruction framework  
63 for Shift-encoded NAVigator-based interleaved EPI at 7 T (dubbed JETS-  
64 NAViEPI). Our pulse sequence, NAViEPI, differs from most existing tech-  
65 niques. First, NAViEPI builds upon interleaved EPI, thereby allowing for  
66 fast and efficient  $k$ -space coverage. Second, inspired by rsEPI, NAViEPI en-  
67 sures the same effective ESP between the imaging and the navigator echo,  
68 thereby minimizing geometric distortion and allowing for the use of a larger  
69 number of shots. NAViEPI essentially integrates the advantages of both iEPI  
70 and rsEPI. Third, NAViEPI utilizes undersampled multi-shot iEPI, thereby  
71 alleviating the SAR problem at 7 T. Fourth, NAViEPI shifts the  $k$ -space in-  
72 plane sampling pattern along the phase encoding ( $k_y$ ) direction. This shifting  
73 creates complementary  $k$ - $q$ -space sampling, which leads to the possibility of  
74 our joint  $k$ - $q$ -slice reconstruction. Specifically, we employ spatial-diffusion  
75 overlapping LLR regularization to jointly reconstruct all diffusion encodings

<sup>76</sup> and multi-band slices. In vivo experiments at 7 T and comparisons with other  
<sup>77</sup> techniques demonstrate the efficiency of our proposed method in achieving  
<sup>78</sup> high spatial resolution DW-MRI at ultra-high field.

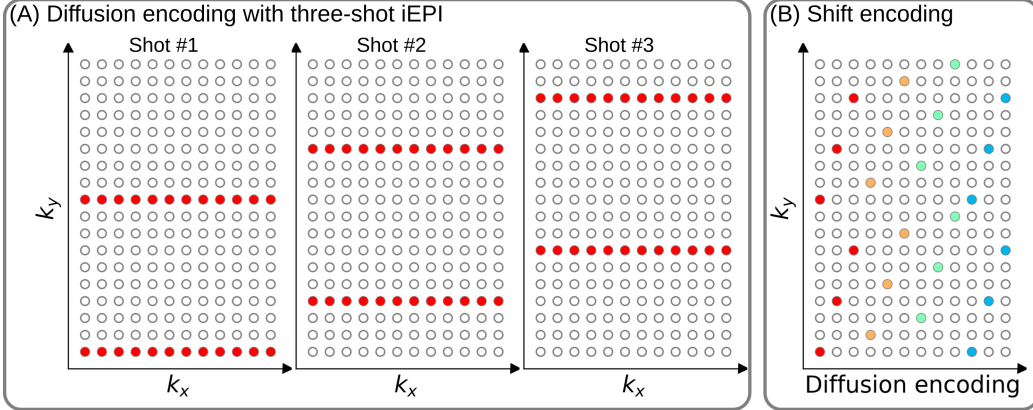


Figure 1: (A) An example DW-MRI acquisition with three-shot interleaved EPI acquisition. (B) The proposed  $k_y$  shifted diffusion encoding scheme. This example employs three shots per DW image. Therefore, every three columns have the same color.

<sup>79</sup> **2. Materials and methods**

<sup>80</sup> *2.1. Multi-band shift-encoded iEPI acquisition*

<sup>81</sup> Fig. 1 (A) displays the diffusion-weighted image acquisition based on  
<sup>82</sup> three-shot interleaved EPI with three-fold in-plane undersampling. Conven-  
<sup>83</sup> tionally, such a sampling pattern is repeated for all diffusion directions. In  
<sup>84</sup> contrast, we propose the  $k_y$ -shifted diffusion encoding, as shown in Fig. 1 (B).  
<sup>85</sup> The interleaved EPI sampling pattern is shifted by one  $k_y$  line per diffusion  
<sup>86</sup> direction, with the cycling period being the in-plane undersampling factor.

<sup>87</sup> It is worth noting that, as shown in Fig. 1 (A), the undersampling factor  
<sup>88</sup> of one segment is  $R_{\text{in-plane}} \times N_{\text{shot}}$  (ignore multi-band undersampling here),  
<sup>89</sup> yielding nine-fold in-plane undersampling in this example. In other words,  
<sup>90</sup> the undersampling factor per segment linearly scales up with the number  
<sup>91</sup> of shots. Consequently, conventional self-gating reconstruction techniques,  
<sup>92</sup> e.g. MUSE, suffer from degraded shot-to-shot phase estimation, which in

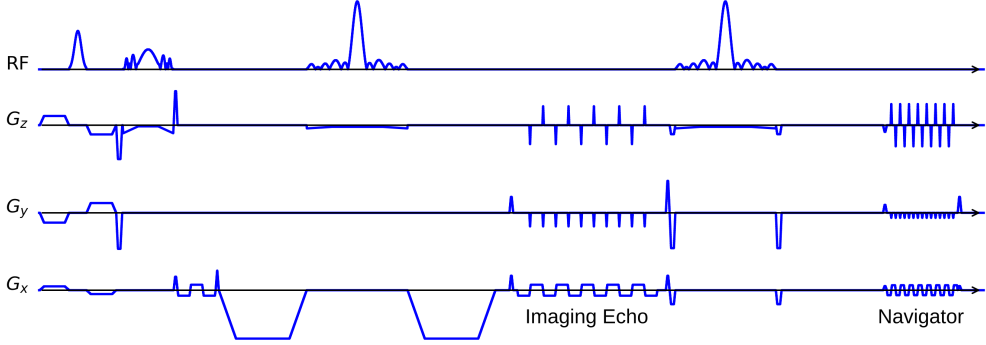


Figure 2: The NAViEPI sequence diagram. SMS is utilized for the acquisition of both imaging and navigator echoes. While the acceleration factor per navigator is the same as listed in Table 1, the acceleration factor per imaging echo is in addition linearly scaled by the number of shots.

93 turn limits the number of shots and spatial resolution.

94 *2.2. NAViEPI: Navigator-based iEPI with consistent effective ESP between  
95 the imaging and the navigator echo - where iEPI meets rsEPI*

96 Instead of the self-gated MUSE with in-plane fully-sampled iEPI and  
97 a limited number of shots, We propose NAVigator-based interleaved EPI  
98 (NAViEPI), as illustrated in Fig. 2. Inspired by rsEPI (Porter and Hei-  
99 demann, 2009), NAViEPI enforces a consistent effective ESP between the  
100 imaging and the navigator echo, thereby minimizing distortion mismatch  
101 between the two echoes.

102 Since one imaging echo presents one segment in multi-shot EPI acquisi-  
103 tion, its effective ESP is defined as

$$\text{ESP}_{\text{eff}} = \frac{\text{ESP}}{R_{\text{in-plane}} \times N_{\text{shot}}} \quad (1)$$

104 Here, a larger number of shots (segments) increases the undersampling factor  
105 per segment (see Fig. 1), but decreases the effective ESP. Since the navigator

106 echo is acquired for each segment, its in-plane undersampling factor equals  
107  $R_{\text{in-plane}}$ . Therefore, the effective ESP of the navigator echo must match that  
108 of the imaging echo, as given in Eq. (1). With a matching effective ESP, the  
109 base resolution of the navigator echo can then be determined.

110 *2.3. In vivo acquisition protocols*

111 We implemented multiple in-vivo acquisition protocols at a clinical 7 T  
112 MR system (MAGNETOM Terra, Siemens Healthineers, Erlangen, Ger-  
113 many) equipped with a 32-channel head coil (Nova Medical, Wilmington,  
114 MA, USA) and the XR-gradient system (maximum gradient strength 80 mT/m  
115 with a peak slew rate of 200 T/m/s). To calibrate coil sensitivity maps, refer-  
116 ence scans employed a gradient-echo (GRE) sequence. Spectral fat saturation  
117 and mono-polar diffusion-encoding gradients were used. The phase-encoding  
118 direction was selected as anterior-to-posterior.

Table 1: NAViEPI acquisition protocols

Protocol	1.0 mm isotropic		sub-millimeter	
	#1	#2	#3	#4
Diffusion mode	MDDW <sup>(1)</sup>		3-scan trace	
Diffusion scheme	monopolar			
Diffusion direction	20	114	3	
<i>b</i> -value (s/mm <sup>2</sup> )	1000	3-shell <sup>(2)</sup>	1000	
<i>b</i> <sub>0</sub>	0	12	1	
FOV (mm <sup>2</sup> )	200	214	220	
In-plane resolution (mm <sup>2</sup> )	1.0		0.5	
Slice thickness (mm)	1.0		2.0	
Slices	141	114	60	
Navigator	No	No	Yes	No
Shots	4	2	5	1
TR (ms)	7700	5200	4400	8000
TEs (ms)	67	66	58/95.1	143
ESP (ms)	1.02	0.81	1.52	1.48
Bandwidth (Hz/Pixel)	1086	1460	758	
Partial Fourier			6/8	
Acceleration <sup>(3)</sup>	1 × 3	3 × 3	3 × 2	
TA (min) <sup>(4)</sup>	10 : 42	22 : 25	1 : 38	0 : 46

<sup>(1)</sup> MDDW: Multi-direction diffusion weighting;

<sup>(2)</sup> 3-shell: 20, 30, and 64 directions with *b*-values of 1000, 2000, and 3000 s/mm<sup>2</sup>, respectively;

<sup>(3)</sup> Acceleration: Both in-plane and slice undersampling can be employed, denoted as (*R*<sub>in-plane</sub> × *R*<sub>slice</sub>);

<sup>(4)</sup> TA: Total acquisition time.

120 This study was approved by the local ethics committee. Three volunteers  
121 with informed consent obtained before scanning participated in this  
122 study. Detailed acquisition protocols are listed in Table 1. In the spirit of re-  
123 producible research, another volunteer with informed consent was recruited  
124 for the scan of all acquisition protocols, and the results were displayed in  
125 Supplementary Information.

126 *2.3.1. 20-diffusion-direction acquisition at 1 mm isotropic resolution*

127 As listed in Table 1, Protocol #1 with four-shot iEPI and without in-  
128 plane undersampling was implemented. This protocol represents the acquisi-  
129 tion scheme employed in many existing multi-shot reconstruction techniques,  
130 (e.g., MUSE, SPA-LLR, and JULEP). The acquired data from this protocol  
131 served as ground truth. Different reconstruction methods, specifically JETS,  
132 MUSE, and JULEP were compared. We compared with JULEP instead of  
133 MUSSELS, because JULEP uses not only structured low-rank constraints  
134 but also explicit phase mapping.

135 We then retrospectively reduced the four-shot data to only one shot per  
136 diffusion encoding without and with the proposed  $k_y$  shifting to simulate  
137 four-fold in-plane undersampling. JETS reconstruction was performed on  
138 the fully-sampled data and the retrospectively undersampled data to validate  
139 the proposed  $k_y$ -shifted acquisition.

140 *2.3.2. Three-shell acquisition at 1 mm isotropic resolution*

141 Protocol #2 in Table 1 was implemented for multi-shell diffusion tensor  
142 imaging (DTI) (Basser et al., 1994). We acquired a total of 114 diffusion  
143 directions, whereas  $b_0$  measurements were interspersed every ten diffusion

<sub>144</sub> directions. This protocol was used to demonstrate the capability of JETS  
<sub>145</sub> in achieving high spatial-angular-temporal resolution.

<sub>146</sub> *2.3.3. 3-scan trace acquisition at  $0.5 \times 0.5 \times 2.0 \text{ mm}^3$  voxel size*

<sub>147</sub> As listed in Table 1, Protocol #3 was implemented based on NAViEPI  
<sub>148</sub> with five shots per diffusion encoding. This protocol was compared against  
<sub>149</sub> single-shot EPI (Protocol #4) with the same spatial resolution and acceler-  
<sub>150</sub> ation, such as to demonstrate the sampling efficiency of NAViEPI.

<sub>151</sub> *2.4. Forward modeling*

<sub>152</sub> Our proposed acquisition method yields multi-dimensional multi-band  
<sub>153</sub>  $k$ -space data  $\mathbf{y}_{c,q,s}$ , where  $c, q, s$  denotes the index of the coil sensitivity  
<sub>154</sub> map, the diffusion encoding, and the shot, respectively. Acquisition modeling  
<sub>155</sub> needs to consider several aspects.

<sub>156</sub> First, the acquired  $k$ -space data  $\mathbf{y}$  is mapped from individual shot images  
<sub>157</sub>  $\mathbf{x}_{q,s,z}$  via the forward model,

$$\begin{aligned} \mathbf{y}_{c,q,s} &= \mathbf{P}_{q,s} \boldsymbol{\Sigma} \boldsymbol{\Theta}_z \mathbf{F} \mathbf{S}_c \mathbf{x}_{q,s,z} \\ \mathbf{y} &:= \mathbf{E}_1 \mathbf{x} \end{aligned} \quad (2)$$

<sub>158</sub> Here, the encoding matrix  $\mathbf{E}_1$  comprises a chain of linear operators. Every  
<sub>159</sub> shot image  $\mathbf{x}$  is point-wise multiplied by a set of coil sensitivity maps ( $\mathbf{S}$ ) and  
<sub>160</sub> Fourier transformed ( $\mathbf{F}$ ). The output is then point-wise multiplied by the  
<sub>161</sub> multi-slice phase map ( $\boldsymbol{\Theta}$ ) with  $z$  the slice index in simultaneously excited  
<sub>162</sub> slices. This operator shifts individual slice along the phase-encoding direction  
<sub>163</sub> via varying phase modulation (Breuer et al., 2005). The SMS  $k$ -space data

164 is then summed (collapsed,  $\Sigma$ ) along the slice dimension and masked (point-  
165 wise multiplied,  $\mathbf{P}$ ) by the sampling pattern of each diffusion encoding and  
166 shot.

167 Second, for diffusion MRI based on multi-shot EPI, multiple shots ac-  
168 quired for a given diffusion encoding need to be combined as one DW image  
169 ( $\tilde{\mathbf{x}}$ ). One possibility is to perform magnitude average (Chen et al., 2013)  
170 or root-sum-squares (RSS) (Mani et al., 2017) of shot images. This method  
171 is robust to in-plane motion, but sub-optimal concerning SNR (Guhaniyogi  
172 et al., 2016). Alternatively, shot combination can be done via shot-to-shot  
173 phase variation correction (Liu et al., 2005; Chen et al., 2013). This can be  
174 incorporated into our formulation as point-wise multiplication between the  
175 shot-to-shot phase variation ( $\Phi$ ) and the DW image ( $\tilde{\mathbf{x}}$ ),

$$\mathbf{x}_{q,s,z} = \Phi_{q,s,z} \tilde{\mathbf{x}}_{q,z} \quad (3)$$

176 Note that  $\tilde{\mathbf{x}}$  can be obtained by applying the adjoint of  $\Phi$  to  $\mathbf{x}$ . In MUSE,  
177  $\Phi$  is obtained by parallel imaging reconstruction of all shots with subsequent  
178 phase smoothing of every shot image. Based on this phase correction, the  
179 complete forward model follows

$$\mathbf{y} := \mathbf{E}_2 \tilde{\mathbf{x}} = \mathbf{E}_1 \Phi \tilde{\mathbf{x}} \quad (4)$$

180 where the encoding matrix  $\mathbf{E}_2$  comprises the chain of the shot-to-shot phase  
181 variation  $\Phi$  and the encoding matrix  $\mathbf{E}_1$ . We implemented these two encoding  
182 operators in SigPy (Ong and Lustig, 2019).

### 183 2.5. Joint $k$ - $q$ -slice reconstruction

184 Based on the generalized forward models in Eqs. (2) and (4), our proposed  
185 joint  $k$ - $q$ -slice reconstruction can be formulated as a three-step approach.

186     **I. Navigator echo reconstruction.** The acquisition of navigator echoes  
 187     follows the forward model in Eq. (2), so the reconstruction of navigator  
 188     echoes can be formulated as:

$$\operatorname{argmin}_{\mathbf{x}} \|\mathbf{y} - \mathbf{E}_1 \mathbf{x}\|_2^2 + \lambda \mathbf{R}(\mathbf{x}) \quad (5)$$

189     where  $\mathbf{R}(\mathbf{x})$  denotes the regularization functional with the regularization  
 190     strength  $\lambda$ . In this work,  $\ell^2$  regularization was used, i.e.,  $\mathbf{R}(\mathbf{x}) =$   
 191      $\|\mathbf{x}\|_2^2$ . In the case of self-navigating (i.e., no navigator acquired) as Pro-  
 192     tocol #2, the central  $k$ -space region (i.e., 1/4 of the full image matrix)  
 193     of each segment is used as  $\mathbf{y}$  in Eq. (5).

194     **II. Phase smoothing.** Shot-to-shot phase variation was extracted from  
 195     the reconstructed navigator echo phases. Assuming that phase images  
 196     are spatially smooth (Chen et al., 2013; Dai et al., 2023), we employed  
 197     the adaptive Hanning filter to smooth shot phases,

$$\mathbf{x} = \mathbf{F}^{-1} \mathcal{H}^K \mathbf{F} \mathbf{x} \quad (6)$$

198     where  $x$  is the reconstructed navigator image from Step I.  $\mathcal{H}$  is the  
 199     Hanning window with the non-negative integer  $K$ .  $K$  controls the width  
 200     of the Hanning window.

201     **III. Shot-combined reconstruction.** Joint reconstruction of all DW im-  
 202     ages using the shot-combined forward model  $\mathbf{E}_2$  with shot-to-shot phase  
 203     variation from Step II reads:

$$\operatorname{argmin}_{\tilde{\mathbf{x}}} \|\mathbf{y} - \mathbf{E}_2 \tilde{\mathbf{x}}\|_2^2 + \lambda \|\mathbf{T}(\tilde{\mathbf{x}})\|_* \quad (7)$$

204     Here, LLR regularization was employed in the local spatial-diffusion  
 205     matrices, based on the theory of partially separable functions (Liang,

206        207; Trzasko and Manduca, 2011; Zhang et al., 2015).  $\mathbf{T}$  represents  
207        a linear operator that firstly slides a local patch window through all  
208        DW images and then flattens every set of local patches to construct  
209        two-dimensional (2D) spatial-diffusion matrices. The spatial dimension  
210        equals the block size, and the diffusion dimension is the number of dif-  
211        fusion encodings.  $\|\mathbf{T}(\tilde{\mathbf{x}})\|_*$  is the nuclear norm, i.e. the sum of singular  
212        values of a spatial-diffusion matrix. This nuclear norm regularization  
213        was accomplished via singular value thresholding (SVT) of each spatial-  
214        diffusion matrix (Cai et al., 2010). After SVT, the adjoint of  $\mathbf{T}$ ,  $\mathbf{T}^H$ ,  
215        was needed to reorder pixel values from the spatial-diffusion matrices  
216        back to DW images.

217        To alleviate checkerboard artifacts induced by LLR regularization with  
218        non-overlapping blocks (Hu et al., 2020), we employed overlapping blocks.  
219        In this case, values from overlapping positions are summed up to the  
220        output of  $\mathbf{T}^H$ . To enable the correct use of  $\mathbf{T}^H$ , we element-wise divided  
221        the output of  $\mathbf{T}^H$  by a scaling matrix. This matrix was obtained via  
222         $\mathbf{T}^H(\mathbf{T}(\mathbf{1}))$ , where  $\mathbf{1}$  denotes the matrix of all ones with the same shape  
223        as the input  $\mathbf{x}$ .

224        As the local patch window varies depending on the number of diffusion R1071.9  
225        encodings or user selection, we implemented a singular-value spectrum  
226        normalization strategy to reduce the effect of the local patch window  
227        variation on regularization strength. Specifically, the singular values of  
228        constructed spatial-diffusion matrices were divided by the patch win-  
229        dow width. After SVT, the thresholded singular values were multiplied  
230        with the patch window width for rescaling.

231    2.6. Reconstruction

232    The acquired raw data was read in by twixtools (<https://github.com/pehses/twixtools>). Ramp-sampling regridding and FOV/2-ghost correction were also performed in twixtools. Subsequently, coil sensitivity maps were computed from reference scans using ESPIRiT (Uecker et al., 2014) in SigPy (Ong and Lustig, 2019).

237    With this pre-processing as well as the implemented forward models and proximal operator, the inverse problem in Eq. (7) was solved by the alternating direction method of multipliers (ADMM) (Boyd et al., 2010).

240    ADMM solves the minimization problems in an alternating update scheme,

$$\begin{cases} \mathbf{x}^{(k+1)} := \underset{\mathbf{x}}{\operatorname{argmin}} \| \mathbf{y} - \mathbf{E}(\mathbf{x}) \|^2 + \rho/2 \| \mathbf{T}\mathbf{x} - \mathbf{z}^{(k)} + \mathbf{u}^{(k)} \|_2^2 \\ \mathbf{z}^{(k+1)} := \mathcal{T}_{\lambda/\rho}(\mathbf{T}\mathbf{x}^{(k+1)} + \mathbf{u}^{(k)}) \\ \mathbf{u}^{(k+1)} := \mathbf{u}^{(k)} + \mathbf{T}\mathbf{x}^{(k+1)} - \mathbf{z}^{(k+1)} \end{cases} \quad (8)$$

241    where  $k$  denotes the ADMM iteration.  $\mathbf{z}$  is the auxiliary variable ( $\mathbf{z} = \mathbf{T}\mathbf{x}$ ), and  $\mathbf{u}$  is the Lagrangian multipliers. Importantly, when solving Eq. (2),  $\mathbf{x}$  denotes shot images and  $\mathbf{E}$  denotes  $\mathbf{E}_1$  in Eq. (8). In contrast,  $\mathbf{x}$  denotes shot-combined images and  $\mathbf{E}$  denotes  $\mathbf{E}_2$  when solving Eq. (4).  $\mathbf{x}$  can be solved using linear least square algorithms, e.g. conjugate gradients (Hestenes and Stiefel, 1952), while  $\mathbf{z}$  is updated via singular value thresholding ( $\mathcal{T}$ ) with the thresholding parameter  $\lambda/\rho$ . The coupling parameter  $\rho$  is effective in both the update of  $\mathbf{x}$  and  $\mathbf{z}$ . It acts as Tikhonov regularization strength when updating  $\mathbf{x}$ , but also inversely scales the thresholding strength when updating  $\mathbf{z}$ .

251    In this work, 15 ADMM iterations with  $\rho = 0.05$  and  $\lambda = 0.01$  were used.

252 All reconstructions were done on a single A100 SXM4/NVLink GPU with  
253 40 GB memory (NVIDIA, Santa Clara, CA, USA).

254 We compared our proposed joint reconstruction with established multi-  
255 shot reconstruction techniques, specifically, MUSE (Chen et al., 2013) and  
256 JULEP (Dai et al., 2023), hosted on GitHub by Dr. Dai (Dai et al., 2023).  
257 Further, we performed the local-PCA denoising (Cordero-Grande et al., 2019)  
258 as implemented in MRtrix (Tournier et al., 2019) on the MUSE reconstructed  
259 complex DW images.

260 The in vivo data acquired from Protocol #2 in Table 1 consisted of 126  
261 diffusion directions, which exceeds the available GPU memory. Therefore,  
262 the 126 data volumes were uniformly split into three parts for our JETS  
263 reconstruction with a LLR block width of 6 and the LLR regularization in  
264 both Steps I and III in Section 2.5. In addition, MUSE reconstruction was  
265 also performed, followed by the local-PCA denoising. Reconstructed DWIs  
266 were then processed by DiPy (Garyfallidis et al., 2014) to obtain color-coded  
267 fractional anisotropy (cFA) maps.

268 **3. Results**

269 *3.1. Smoothing of shot-to-shot phase variation*

270 Navigators were acquired with the acceleration rate as listed in Table 1.  
271 Besides, the base resolution of navigators (e.g. 32 in Protocol #3 in Table 1)  
272 was smaller than imaging echoes. As a result, reconstructed navigator phases  
273 (refer to the first column in Fig. 3) from Step I in Section 2.5 are not spatially  
274 smooth. Such phases, when used in the shot-combined reconstruction, result  
275 in signal void artifacts in DW images. To address this problem, we utilized  
276 the phase smoothing procedure. As shown in Fig. 3, the ripple-like phase  
277 artifact disappears at  $K = 5$ , while retaining the shot-to-shot phase variation.  
278 In contrast, a larger  $K$  (e.g.,  $K = 20$ ) makes the filter too strong and partially  
279 removes phase variation.

R1071.12

280 *3.2. Comparison to MUSE and JULEP with four-shot iEPI acquisition*

281 The iterative phase smoothing was also applicable to MUSE-type self-  
282 navigating reconstruction, where shot phases were reconstructed from imag-  
283 ing echoes. Fig. 4 compares our proposed JETS with MUSE (Chen et al.,  
284 2013), MUSE with complex-valued local-PCA denoiser (Cordero-Grande et al.,  
285 2019), and JULEP (Dai et al., 2023). The residual noise from MUSE can be  
286 largely removed by the denoiser. However, when compared to JETS, the de-  
287 noiser shows residual noise patterns within the globus pallidus (indicated by  
288 the red arrow). JETS also shows better denoising than JULEP. The reason  
289 is that JETS enforces spatial-diffusion regularization, whereas JULEP for-  
290 mulates structured low-rank regularization of the four shots for one diffusion  
291 encoding.

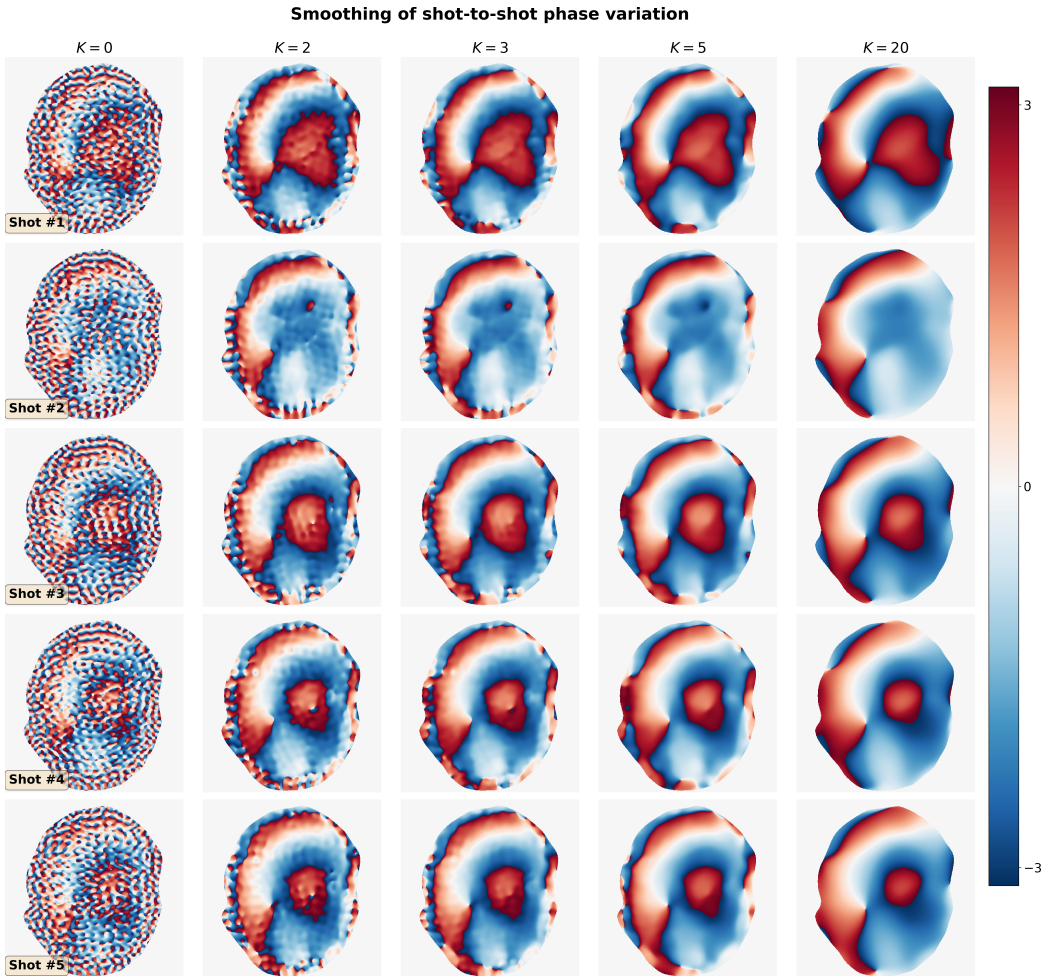


Figure 3: Smoothing of shot-to-shot phase variation according to Eq. (6). Navigators from Protocol #3 were reconstructed based on Step I in Section 2.5 and then used as the input (the column with  $K = 0$ ).

**8th DW image from 4-shot iEPI @ 1 mm ISO**

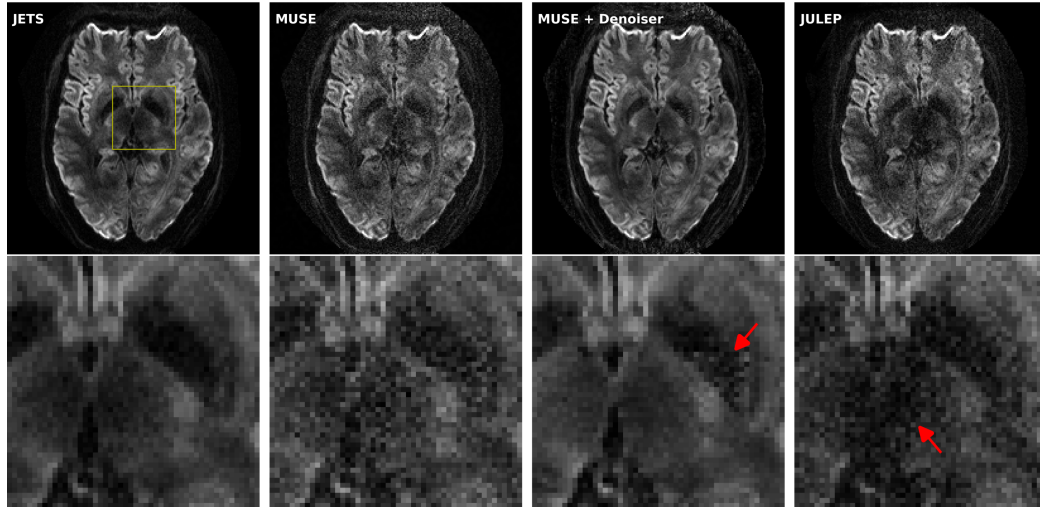


Figure 4: Reconstructed DW images (the 8th diffusion encoding) based on 4-shot iEPI acquisition with 1 mm isotropic resolution (Protocol #1 in Table 1). Four reconstruction methods are compared (from left to right): JETS, MUSE, MUSE with denoiser, and JULEP. The 2nd row displays the magnified views of the yellow square. The image from the denoiser (3rd column) shows residual noise patterns within the globus pallidus (indicated by the red arrow). The JULEP reconstruction (4th column) shows signal dropout in the central region (indicated by the red arrow).

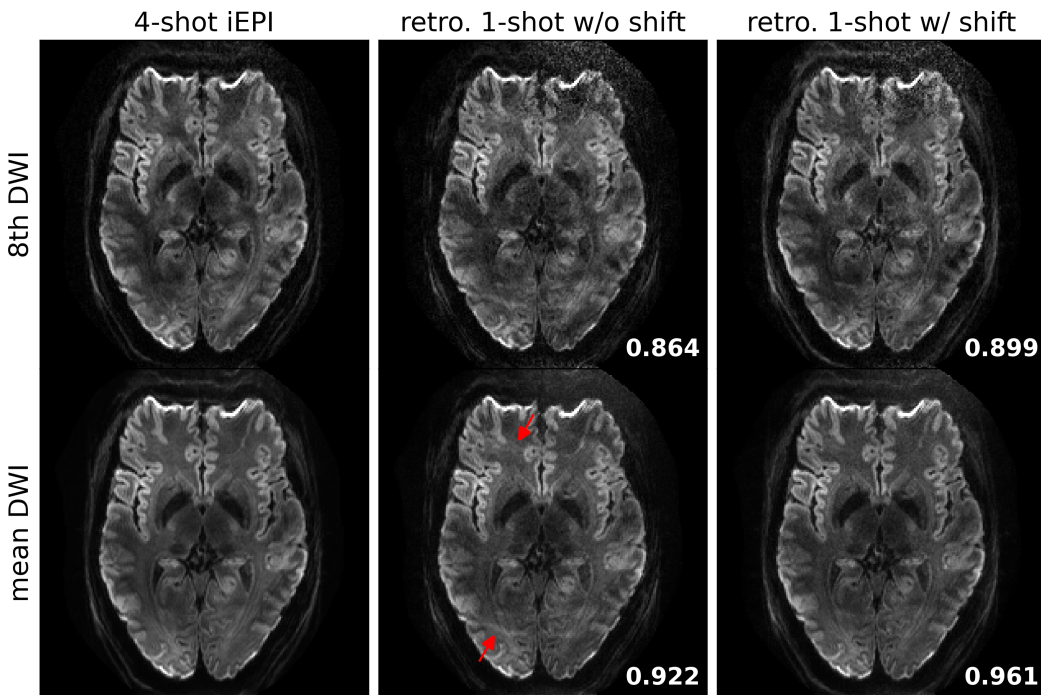


Figure 5: Quantitative validation of the proposed  $k_y$ -shift encoding sampling pattern based on 4-shot iEPI acquisition with 1 mm isotropic resolution (Protocol #1 in Table 1). (Top) the 8th diffusion encoding and (bottom) mean DWI over 20 diffusion encodings. (1st column) JETS reconstruction of 4-shot iEPI acquisition is used as the ground truth. The 2nd and the 3rd column displays JETS reconstruction of retrospectively undersampled 1-shot acquisition without and with  $k_y$  shifting, respectively. Residual aliasing artifacts are visible in the reconstruction without  $k_y$  shifting, as indicated by the red arrows. Structural similarity (SSIM) values are computed and displayed in the bottom right corners.

292    3.3. Retrospectively undersampling from the four-shot iEPI acquisition

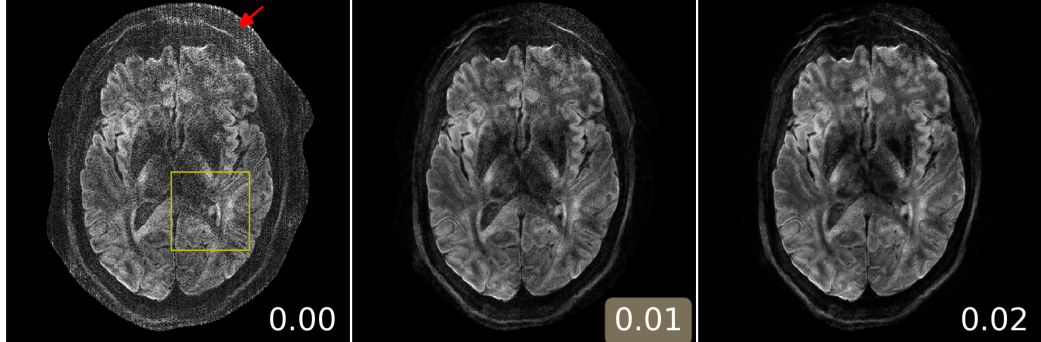
293    JETS reconstruction results on the four-shot prospectively fully-sampled  
294    data from Protocol #1 in Table 1, as well as on the retrospectively under-  
295    sampled one-shot data without and with the proposed  $k_y$  shift are displayed  
296    in Fig. 5. Residual aliasing artifacts are visible in the reconstruction with-  
297    out  $k_y$  shifting, as indicated by the red arrows. In contrast, the  $k_y$  shifting  
298    scheme supplies a complementary  $k$ - $q$ -space sampling pattern, which is bene-  
299    ficial for joint reconstructions such as JETS. As shown in Fig. 5, JETS results  
300    in improved SSIM values and reduced aliasing artifacts, when compared to  
301    the reconstruction without  $k_y$  shifting. Figs. 4 and 5 show a slice containing  
302    the globus pallidus with strong  $T_2$ -weighted contrast and highlighting the  
303    advantage of  $k_y$ -shift encoding in reducing undersampling artifacts.

304    3.4. Analysis of reconstruction parameters

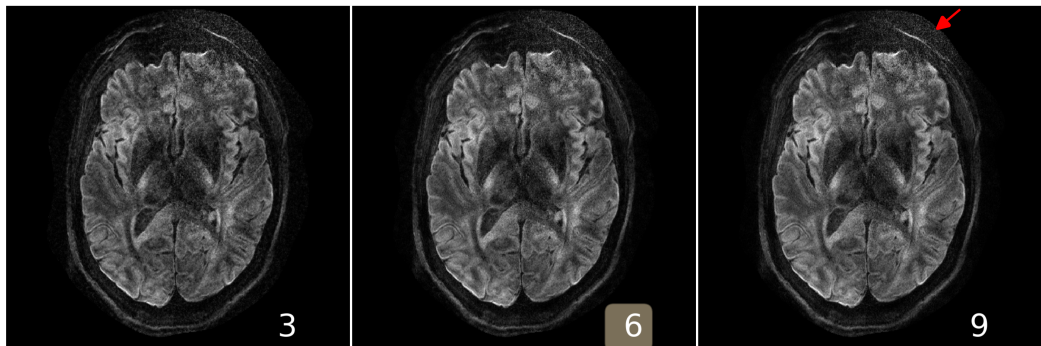
305    Here we provide a systematic analysis of the proposed JETS reconstruc-  
306    tion with LLR regularization applied to the spatial-diffusion dimension, as  
307    shown in Fig. 6.

308    First, we varied the regularization strength  $\lambda$ . We tested values of 0, 0.08,  
309    and 0.16. The reconstruction with  $\lambda = 0$  in Eq. (7) corresponds to parallel  
310    imaging reconstruction without LLR regularization. It is worth noting that  
311    the proposed NAViEPI sequence demonstrates high-quality sub-millimeter  
312    DW images ( $0.5 \times 0.5 \times 2.0$  mm $^3$  in this example). The DW images can be  
313    further improved with the use of LLR regularization, i.e., reduced noise, as  
314    seen in the reconstruction with  $\lambda = 0.01$ . Increasing  $\lambda$  (e.g. 0.02) further  
315    reduces noise, but at the cost of increased blurring. Therefore,  $\lambda = 0.01$  was  
316    selected in this work.

**(A) varying  $\lambda$ , keeping block as 6 and stride as 1**



**(B) varying block width, keeping  $\lambda$  0.01 and stride as 1**



**(C) varying stride, keeping  $\lambda$  as 0.01 and block as 6**

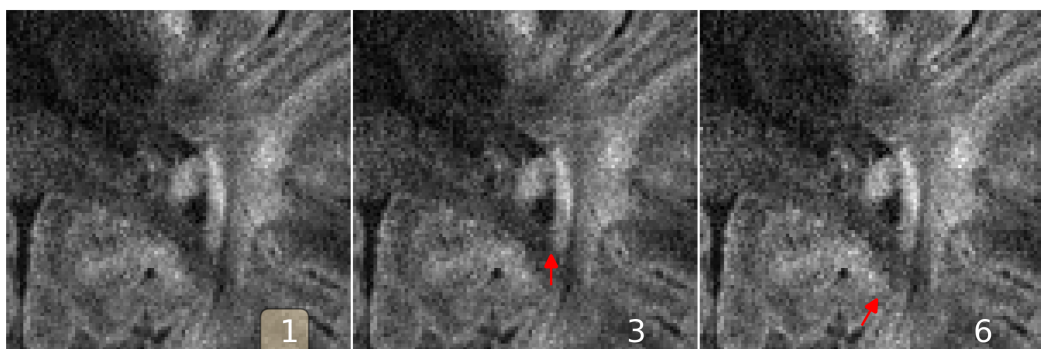


Figure 6: Analysis of reconstruction parameters based on the 3-scan trace acquisition with  $0.5 \times 0.5 \times 2.0 \text{ mm}^3$  (Protocol #3 in Table 1). Displayed are JETS reconstructed single-direction DW images. **(A)** Varying the regularization strength  $\lambda$  from 0 to 0.01 and 0.02. **(B)** Varying the block width from 3 to 6 and 9. The red arrow indicates increased noise with the large block width. **(C)** Varying the stride size from 1 to 3 (partially overlapping) and 6 (non-overlapping). The red arrows indicate blocky artifacts.

317 Second, besides the regularization strength, the block size (i.e., the area  
318 of 2D patches) also plays a role in denoising. We employed square blocks in  
319 this work. Here, the block width of 3 shows the best denoising as compared  
320 to 6 and 9, especially in the peripheral brain region.

321 Third, we varied the stride, i.e., the step from one local patch to the  
322 next. The use of overlapping LLR (Fig. 6 (C) left) better suppresses blocky  
323 artifacts, compared to the partially overlapping (stride < block) LLR (Fig. 6  
324 (C) middle) and the non-overlapping (stride = block) LLR (Fig. 6 (C) right).

325 *3.5. Sampling efficiency of NAViEPI*

326 As shown in Fig. 7, NAViEPI achieves sub-millimeter resolution (voxel  
327 size  $0.5 \times 0.5 \times 2.0 \text{ mm}^3$ ) with the use of a 5-shot acquisition. When compared  
328 to a single-shot acquisition with the same voxel size, the acquisition time of  
329 NAViEPI is about two times longer, but the image quality of NAViEPI is  
330 remarkably improved.

331 In the sub-millimeter imaging scenario, the increased base resolution re-  
332 quires longer TE (143 ms) in the single-shot acquisition, which results in  
333 significant signal loss due to  $T_2$  relaxation. Therefore, sub-millimeter DWI  
334 necessitates multi-shot acquisition, which is subject to shot-to-shot phase  
335 variation and long scan time. However, NAViEPI solves both challenges. The  
336 5-shot acquisition reduces TE to 58 ms, and thus retains SNR significantly  
337 compared to the single-shot acquisition. Moreover, the JETS reconstruction  
338 can help to reduce noise and improve structural visibility.

339 Fig. 8 shows the JETS reconstructed  $b_0$  and TRACE images in different  
340 slice locations. Admittedly, the lower brain region (e.g. slice #22) exhibits in-  
341 homogeneous and lower signal intensity than the upper slices. Such inhomog-

**3-scan trace acquisition with voxel size  $0.5 \times 0.5 \times 2.0 \text{ mm}^3$**

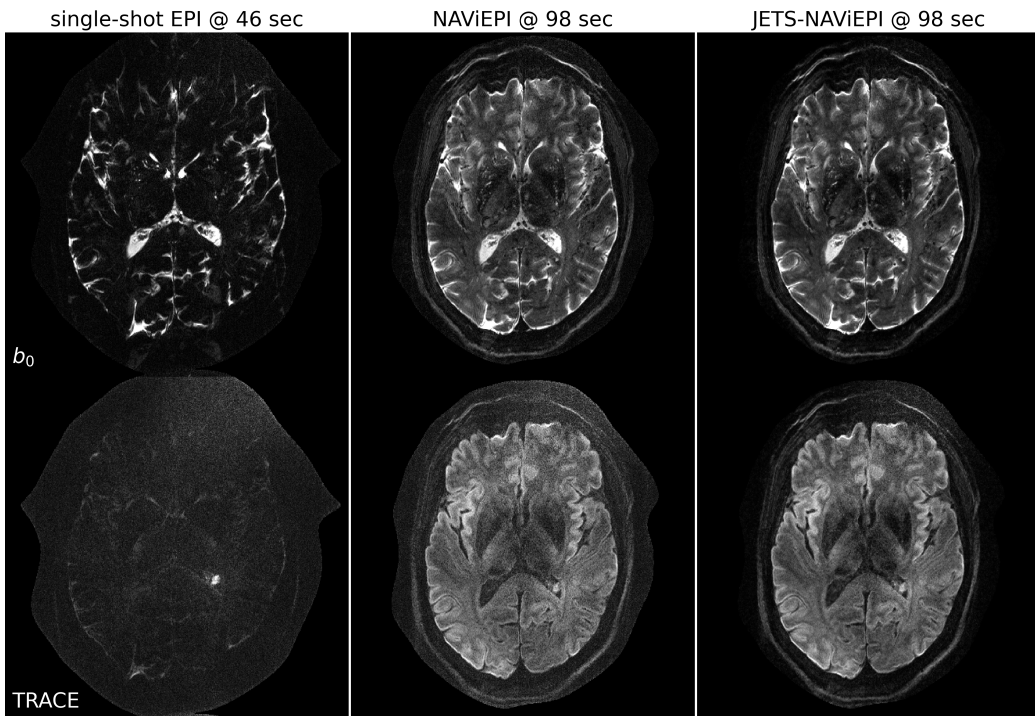


Figure 7: Sampling efficiency of the proposed NAViEPI sequence. 5-shot NAViEPI acquisition with the voxel size  $0.5 \times 0.5 \times 2.0 \text{ mm}^3$  (Protocol #3) was compared with single-shot EPI acquisition (Protocol #4). Both the 1st and the 2nd columns were reconstructed via parallel imaging without LLR regularization, whereas the 3rd column was reconstructed via JETS.

**3-scan trace acquisition with voxel size  $0.5 \times 0.5 \times 2.0 \text{ mm}^3$**

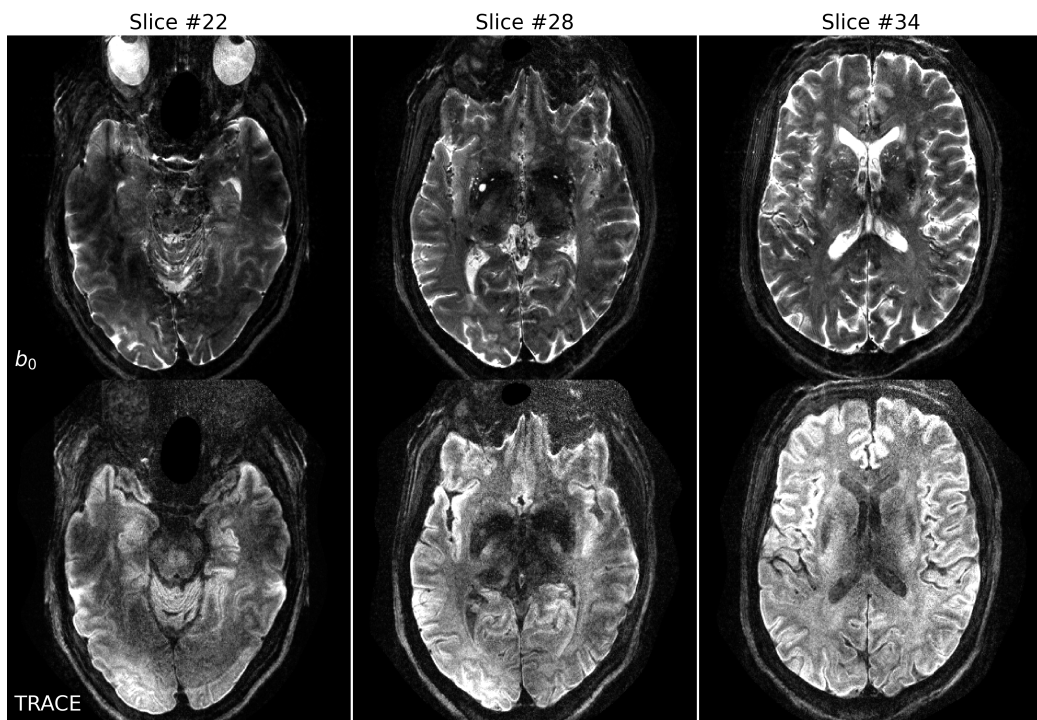


Figure 8: Reconstruction of the 3-scan trace acquisition with the voxel size  $0.5 \times 0.5 \times 2.0 \text{ mm}^3$  (Protocol #3) at different slices.

342 geneity can be alleviated with the use of multi-channel parallel transmission  
343 (Katscher et al., 2003; Grissom et al., 2010).

344 Here, Figs. 6 and 7 show a slice with a benign lesion (the circular bright R1071.7  
345 spot) within the left ventricle. Fig. 8 displays three representative slices:  
346 (left) an inferior brain region with marked  $B_1^+$  field inhomogeneity, (mid-  
347 dle) the middle brain slice which shows susceptibility artifacts in the frontal  
348 region, and (right) a superior brain slice which shows the ventricle.

349 *3.6. Diffusion tensor imaging*

350 Protocol #2 in Table 1 yields an acceleration factor of  $6 \times 3$  per shot, re-  
351 sulting in severe noise amplification in MUSE reconstructed DWIs, as shown  
352 in Fig. 9. Here, a slice that highlights the corpus callosum is displayed, and  
353 the diffusion direction at the  $b$ -value of  $3000 \text{ s/mm}^2$  with bright signal within  
354 the corpus callosum is shown. The local-PCA denoiser substantially removes  
355 noise, but the DWI at high  $b$ -values still illustrates more noise, compared to  
356 the proposed JETS reconstruction. On the other hand, we applied the local-  
357 PCA denoiser before the shot combination in MUSE. As shown in Fig. 9,  
358 this approach is less effective compared to the application of the denoiser  
359 after the shot combination, because shot images were reconstructed from the  
360 central  $k$ -space region and have a coarse resolution.

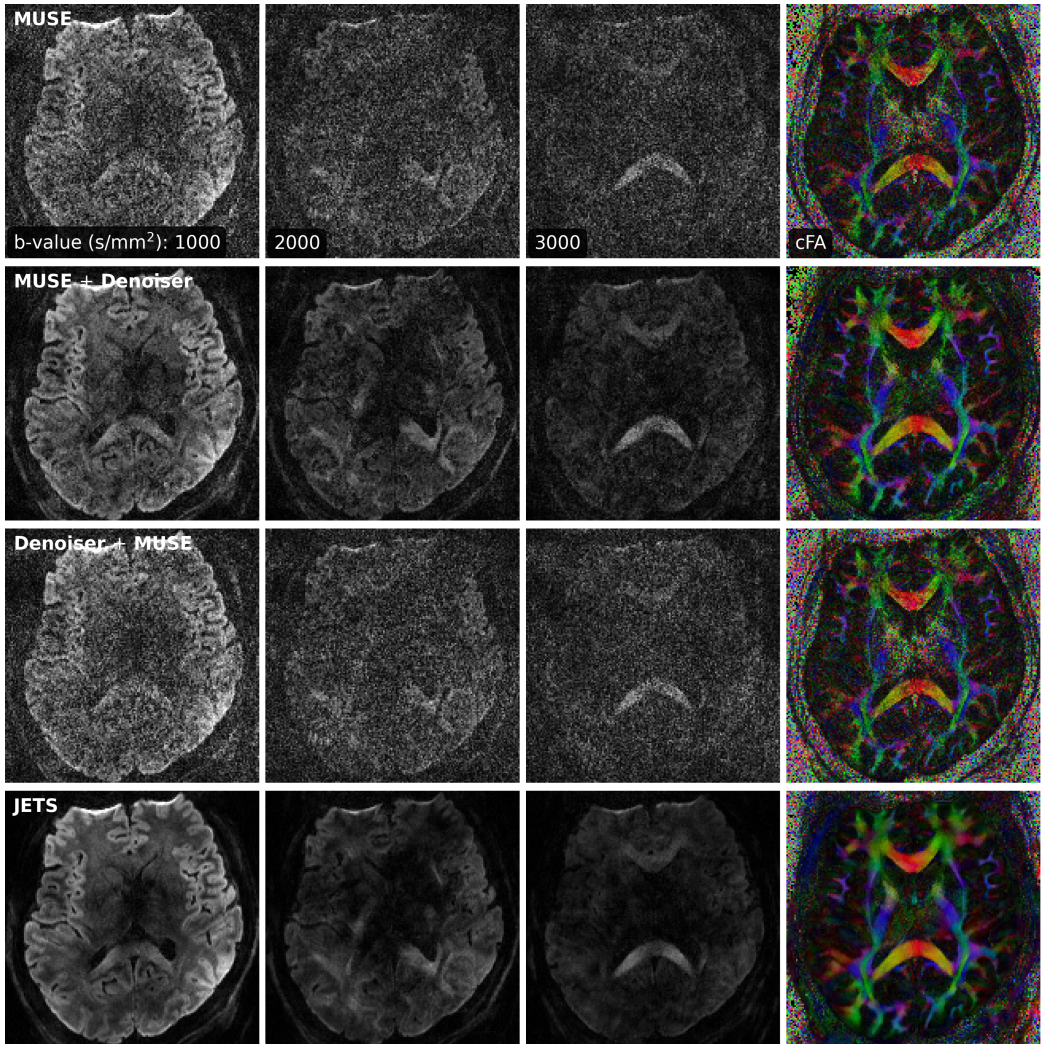


Figure 9: Comparison of three-shell DWIs and cFA maps with data acquired by Protocol #2 in Table 1. Reconstruction methods from top to bottom were MUSE, MUSE with the local-PCA denoiser, the application of the denoiser on shot images before the shot combination in MUSE, and the proposed JETS method.

361    **4. Discussion**

362    This work reports a novel DW-MRI technique, JETS-NAViEPI. NAViEPI  
363    (1) achieves the fast and efficient acquisition of both imaging and navigator  
364    echoes, (2) enforces consistent effective ESP between the two echoes, and (3)  
365    allows for undersampled iEPI as well as a large number of shots. Moreover,  
366    compared to the single-shot acquisition, joint  $k$ - $q$ -slice reconstruction with  $k_y$ -  
367    shift encoding on NAViEPI retains SNR and reduces aliasing artifacts in DW  
368    images. As a result, JETS-NAViEPI renders high spatiotemporal resolution  
369    diffusion MRI protocols in 7 T, e.g., a 3-scan trace acquisition with the voxel  
370    size  $0.5 \times 0.5 \times 2.0 \text{ mm}^3$  at 1.5 min.

371    One limitation of JETS-NAViEPI is the long reconstruction time due to  
372    the simultaneous reconstruction of all DW images and the use of overlapping  
373    locally low-rank regularization. The reconstruction for the Protocol #3 in  
374    Table 1 on an A100 GPU takes about 2 min per multi-band slice. To reduce  
375    the computation time, coil compression algorithms (Buehrer et al., 2007;  
376    Huang et al., 2008) can be employed to reduce the number of coils for image  
377    reconstruction. Moreover, one can deploy multi-GPU distributed computing  
378    or modern optimization algorithms (e.g. stochastic gradient descent) (Ong  
379    et al., 2020) to speed up the reconstruction.

380    Neither the signal modeling in Eqs. (2) and (4) nor the LLR regularization  
381    considers the subject motion. In the presence of motion, the regularized  
382    reconstruction can degrade. To overcome this problem, scout-informed mo-  
383    tion estimation and reconstruction (Polak et al., 2022) could be integrated  
384    into the framework.

385    Another potential extension of this work is to incorporate distortion cor-

386 rection. The standard distortion correction method is known as TOPUP  
387 (Andersson et al., 2003), which acquires two scans with opposing phase-  
388 encoding directions to obtain the field inhomogeneity map and then per-  
389 forms conjugate phase reconstruction to correct for distortion. Alternatively,  
390 a multi-echo acquisition could be used for the coil sensitivity reference scan,  
391 such that both coil sensitivity and  $B_0$  field inhomogeneity maps could be  
392 reconstructed from the data.

393 This work employed a single regularization weight  $\lambda$  to enforce low rank-  
394 ness along the spatial-diffusion direction. However, SNR may be heteroge-  
395 neous within the FOV. Therefore, one single regularization scalar may be  
396 inadequate to cover the whole FOV. Beyond this SVT-based reconstruction,  
397 one can seek to use machine learning to learn a  $q$ -space prior as the regularizer  
398 (Hammernik et al., 2018; Lam et al., 2019; Mani et al., 2021).

399 Although NAViEPI employs navigators for the acquisition of shot-to-  
400 shot phase variation, it is worth noting that phase behavior depends on  
401 several hard-to-control factors such as pulsatile motion, bulk motion, loca-  
402 tions within the brain, and diffusion sensitization strength. Therefore, more  
403 comprehensive modeling or post-processing such as image registration can  
404 be considered in future work.

405 This work compared LLR regularized JETS to MUSE post-processed by  
406 the local PCA denoiser (Cordero-Grande et al., 2019). Both the LLR regular-  
407 ization and the local PCA denoiser are based on the principle that low rank-  
408 ness exists in the spatial-diffusion dimension (Moeller et al., 2021), where the  
409 spatial content is extracted from local patches within the full image volume  
410 and the diffusion dimension is from the  $q$ -space encoding. One could integrate

R990.3.b.2

411 the automatic noise estimation based on the Marchenko-Pastur law for the  
412 determination of the thresholds in the LLR regularization to synergize these  
413 two methods.

414 While this work reconstructs all DW images and then performs model  
415 fitting, an alternative approach is to directly estimate  $b_0$  and diffusion ten-  
416 sors from measured  $k$ - $q$ -space data using model-based reconstruction (Knoll  
417 et al., 2015; Dong et al., 2018; Shafieizargar et al., 2023). Compared to DW  
418 image reconstruction, model-based reconstruction solves for a fewer number  
419 of unknowns, but requires strict diffusion tensor modeling and the use of  
420 nonlinear least square solvers.

421 **5. Conclusions**

422 We demonstrated the JETS-NAViEPI technique, which integrates a  $k_y$ -  
423 shifted encoding navigator-based interleaved EPI sequence and joint recon-  
424 struction with overlapping locally low-rank regularization for high spatial-  
425 angular-temporal resolution DW-MRI at 7 T. This technique allows for high-  
426 quality DW image reconstruction with accelerated acquisitions.

427 **Funding**

428 Funding by the German Research Foundation (DFG) is gratefully ac-  
429 knowledged (projects 513220538, 512819079; and project 500888779 of the  
430 RU5534 MR biosignatures at UHF). In addition, funding by the National  
431 Institutes of Health (NIH), R01 EB024532 and P41 EB017183, is gratefully  
432 acknowledged.

433 In addition, we gratefully acknowledge the scientific support and HPC  
434 resources provided by the Erlangen National High Performance Computing  
435 Center (NHR@FAU) of Friedrich-Alexander-University Erlangen-Nuremberg  
436 (FAU) under the NHR project b143dc. NHR funding is provided by federal  
437 and Bavarian state authorities. NHR@FAU hardware is partially funded by  
438 the German Research Foundation (DFG) – 440719683.

439 **Data and code available statement**

440 In the spirit of reproducible and open science, we publish our source  
441 code (<https://github.com/ZhengguoTan/sigpy>) as well as the raw  $k$ -space  
442 data (<https://doi.org/10.5281/zenodo.7548595>). We also provide inter-  
443 active demonstrations of the reconstruction procedure ([https://github.com/ZhengguoTan/demo\\_jets\\_diffusion\\_mri\\_7t](https://github.com/ZhengguoTan/demo_jets_diffusion_mri_7t)).

445 **Acknowledgments**

446 The authors thank Dr. Peter Neher for the discussion on MITK-Diffusion.  
447 The authors thank Dr. Berkin Bilgic for making the MUSSELS source code  
448 (<https://bit.ly/2QgBg9U>) publically available, Dr. Erpeng Dai for sharing  
449 the JULEP source code (<https://github.com/daiep/JULEP>) on GitHub,  
450 and Dr. Zhiyong Zhang for sharing the SPA-LLR source code (<https://github.com/ZZgroupSJTU/PMCmsDTI>) on GitHub. The authors also thank  
451 Dr. Philipp Ehses for the discussion on twixtools (<https://github.com/pehses/twixtools>).  
452

454 **References**

- 455 Andersson, J.L.R., Skare, S., Ashburner, J., 2003. How to correct suscepti-  
456 bility distortions in spin-echo echo-planar images: application to diffusion  
457 tensor imaging. NeuroImage 20, 870–888. doi:[10.1016/S1053-8119\(03\)00336-7](https://doi.org/10.1016/S1053-8119(03)00336-7).
- 459 Bammer, R., Keeling, S.L., Augustin, M., Pruessmann, K.P., Wolf, R., Stoll-  
460 berger, R., Hartung, H.P., Fazekas, F., 2001. Improved diffusion-weighted  
461 single-shot echo-planar imaging (EPI) in stroke using sensitivity encoding  
462 (SENSE). Magn. Reson. Med. 46, 548–554. doi:[10.1002/mrm.1226](https://doi.org/10.1002/mrm.1226).
- 463 Basser, P.J., Mattiello, J., Le Bihan, D., 1994. MR diffusion tensor  
464 spectroscopy and imaging. Biophys. J. 66, 259–267. doi:[10.1016/S0006-3495\(94\)80775-1](https://doi.org/10.1016/S0006-3495(94)80775-1).
- 466 Bilgic, B., Chatnuntawech, I., Manhard, M.K., Tian, Q., Liao, C., Iyer, S.S.,  
467 Cauley, S.F., Huang, S.Y., Polimeni, J.R., Wald, L.L., Setsompop, K.,  
468 2019. Highly accelerated multishot echo planar imaging through synergistic  
469 machine learning and joint reconstruction. Magn. Reson. Med. 82, 1343–  
470 1358. doi:[10.1002/mrm.27813](https://doi.org/10.1002/mrm.27813).
- 471 Block, K.T., Uecker, M., Frahm, J., 2007. Undersampled radial MRI with  
472 multiple coils. Iterative image reconstruction using a total variation con-  
473 straint. Magn. Reson. Med. 57, 1186–1098. doi:[10.1002/mrm.21236](https://doi.org/10.1002/mrm.21236).
- 474 Boyd, S., Parikh, N., Chu, E., Peleato, B., Eckstein, J., 2010. Distributed  
475 optimization and statistical learning via the alternating direction method

- 476 of multipliers. Foundations and Trends in Machine Learning 3, 1–122.  
477 doi:[10.1561/2200000016](https://doi.org/10.1561/2200000016).
- 478 Breuer, F.A., Blaimer, M., Heidemann, R.M., Mueller, M.F., Griswold, M.A.,  
479 Jakob, P.M., 2005. Controlled aliasing in parallel imaging results in higher  
480 acceleration (CAPIRINHA) for multi-slice imaging. Magn. Reson. Med.  
481 53, 684–691. doi:[10.1002/mrm.20401](https://doi.org/10.1002/mrm.20401).
- 482 Buehrer, M., Pruessmann, K.P., Boesiger, P., Kozerke, S., 2007. Array com-  
483 pression for MRI with large coil arrays. Magn. Reson. Med 57, 1131–1139.  
484 doi:[10.1002/mrm.21237](https://doi.org/10.1002/mrm.21237).
- 485 Butts, K., Riederer, S.J., Ehman, R.L., Thompson, R.M., Jack, C.R., 1993.  
486 Interleaved echo planar imaging on a standard MRI system. Magn. Reson.  
487 Med. 31, 67–72. doi:[10.1002/mrm.1910310111](https://doi.org/10.1002/mrm.1910310111).
- 488 Cai, J.F., Candès, E.J., Shen, Z., 2010. A singular value threshold-  
489 ing algorithm for matrix completion. SIAM. J. Optim. 20, 1956–1982.  
490 doi:[10.1137/080738970](https://doi.org/10.1137/080738970).
- 491 Chen, N.K., Guidon, A., Chang, H.C., Song, A.W., 2013. A robust multi-  
492 shot scan strategy for high-resolution diffusion weighted MRI enabled by  
493 multiplexed sensitivity-encoding (MUSE). NeuroImage 72, 41–47. doi:[10.1016/j.neuroimage.2013.01.038](https://doi.org/10.1016/j.neuroimage.2013.01.038).
- 495 Cordero-Grande, L., Christiaens, D., Hutter, J., Price, A.N., Hajnal, J.V.,  
496 2019. Complex diffusion-weighted image estimation via matrix recovery  
497 under general noise models. NeuroImage 200, 391–404. doi:[10.1016/j.neuroimage.2019.06.039](https://doi.org/10.1016/j.neuroimage.2019.06.039).

- 499 Dai, E., Ma, X., Zhang, Z., Yuan, C., Guo, H., 2017. Simultaneous multislice  
500 accelerated interleaved EPI DWI using generalized blipped-CAIPI acqui-  
501 sition and 3D K-space reconstruction. Magn. Reson. Med. 77, 1593–1605.  
502 doi:[10.1002/mrm.26249](https://doi.org/10.1002/mrm.26249).
- 503 Dai, E., Mani, M., McNab, J.A., 2023. Multi-band multi-shot diffu-  
504 sion MRI reconstruction with joint usage of structured low-rank con-  
505 straints and explicit phase mapping. Magn. Reson. Med. 89, 95–111.  
506 doi:[10.1002/mrm.29422](https://doi.org/10.1002/mrm.29422).
- 507 Dai, E., Zhang, Z., Ma, X., Dong, Z., Li, X., Xiong, Y., Yuan, C., Guo, H.,  
508 2018. The effects of navigator distortion and noise level on interleaved EPI  
509 DWI reconstruction: a comparison between image- and *k*-space method.  
510 Magn. Reson. Med. 80, 2024–2032. doi:[10.1002/mrm.27190](https://doi.org/10.1002/mrm.27190).
- 511 Dong, Z., Dai, E., Wang, F., Zhang, Z., Ma, X., Yuan, C., Guo, H., 2018.  
512 Model-based reconstruction for simultaneous multislice and parallel imag-  
513 ing accelerated multishot diffusion tensor imaging. Med. Phys. 45, 3196–  
514 3204. doi:[10.1002/mp.12974](https://doi.org/10.1002/mp.12974).
- 515 Garyfallidis, E., Brett, M., Amirbekian, B., Rokem, A., van der Walt, S.,  
516 Descoteaux, M., Nimmo-Smith, I., Contributors, D., 2014. DIPY, a library  
517 for the analysis of diffusion MRI data. Front. Neuroinform. 8, 1–17. doi:[10.3389/fninf.2014.00008](https://doi.org/10.3389/fninf.2014.00008).
- 519 Grissom, W.A., Sacolick, L., Vogel, M.W., 2010. Improving high-field MRI  
520 using parallel excitation. Imaging Med. 2, 675–693. doi:[10.2217/IIM.10.62](https://doi.org/10.2217/IIM.10.62).

- 522 Griswold, M.A., Jakob, P.M., Heidemann, R.M., Nittka, M., Jellus, V.,  
523 Wang, J., Kiefer, B., Haase, A., 2002. Generalized autocalibrating par-  
524 tially parallel acquisitions (GRAPPA). Magn. Reson. Med. 47, 1202–1210.  
525 doi:[10.1002/mrm.10171](https://doi.org/10.1002/mrm.10171).
- 526 Guhaniyogi, S., Chu, M.L., Chang, H.C., Song, A.W., Chen, N.K., 2016. Mo-  
527 tion immune diffusion imaging using augmented MUSE for high-resolution  
528 multi-shot EPI. Magn. Reson. Med. 75, 639–652. doi:[10.1002/mrm.25624](https://doi.org/10.1002/mrm.25624).
- 529 Hammernik, K., Klatzer, T., Kobler, E., Recht, M.P., Sodickson, D.K., Pock,  
530 T., Knoll, F., 2018. Learning a variational network for reconstruction of  
531 accelerated MRI data. Magn. Reson. Med. 79, 3055–3071. doi:[10.1002/mrm.26977](https://doi.org/10.1002/mrm.26977).
- 533 Heidemann, R.M., Porter, D.A., Anwander, A., Feiweier, T., Heberlein, K.,  
534 Knösche, T.R., Turner, R., 2010. Diffusion imaging in humans at 7 T  
535 using readout-segmented EPI and GRAPPA. Magn. Reson. Med. 64, 9–  
536 14. doi:[10.1002/mrm.22480](https://doi.org/10.1002/mrm.22480).
- 537 Hestenes, M.R., Stiefel, E., 1952. Methods of conjugate gradients for solving  
538 linear systems. J. Res. Natl. Bur. Stand. 49, 409–436. doi:[10.6028/jres.049.044](https://doi.org/10.6028/jres.049.044).
- 540 Hu, Y., Wang, X., Tian, Q., Yang, G., Daniel, B., McNab, J., Hargreaves, B.,  
541 2020. Multi-shot diffusion-weighted MRI reconstruction with magnitude-  
542 based spatial-angular locally low-rank regularization (SPA-LLR). Magn.  
543 Reson. Med. 83, 1596–1607. doi:[10.1002/mrm.28025](https://doi.org/10.1002/mrm.28025).

- 544 Huang, F., Vijayakumar, S., Li, Y., Hertel, S., Duensing, G.R., 2008. A soft-  
545 ware channel compression technique for faster reconstruction with many  
546 channels. *Magn. Reson. Imaging* 26, 133–141. doi:[10.1016/j.mri.2007.04.010](https://doi.org/10.1016/j.mri.2007.04.010).
- 548 Jeong, H.K., Gore, J.C., Anderson, A.W., 2013. High-resolution human  
549 diffusion tensor imaging using 2-D navigated multishot SENSE EPI at 7  
550 T. *Magn. Reson. Med.* 69, 793–802. doi:[10.1002/mrm.24320](https://doi.org/10.1002/mrm.24320).
- 551 Jones, D.K., 2010. Diffusion MRI: Theory, methods, and applications. Oxford  
552 University Press. doi:[10.1093/med/9780195369779.001.0001](https://doi.org/10.1093/med/9780195369779.001.0001).
- 553 Katscher, U., Börnert, P., Leussler, C., van den Brink, J.S., 2003. Transmit  
554 SENSE. *Magn. Reson. Med.* 49, 144–150. doi:[10.1002/mrm.10353](https://doi.org/10.1002/mrm.10353).
- 555 Knoll, F., Raya, J.G., Halloran, R.O., Baete, S., Sigmund, E., Bammer, R.,  
556 Block, T., Otazo, R., Sodickson, D.K., 2015. A model-based reconstruction  
557 for undersampled radial spin-echo DTI with variational penalties on the  
558 diffusion tensor. *NMR Biomed* 28, 353–366. doi:[10.1002/nbm.3258](https://doi.org/10.1002/nbm.3258).
- 559 Lam, F., Li, Y., Peng, X., 2019. Constrained magnetic resonance spectro-  
560 scopic imaging by learning nonlinear low-dimensional models. *IEEE Trans.*  
561 *Med. Imaging* 39, 545–555. doi:[10.1109/TMI.2019.2930586](https://doi.org/10.1109/TMI.2019.2930586).
- 562 Le Bihan, D., Breton, E., Lallemand, D., Grenier, P., Cabanis, E., Laval-  
563 Jeantet, M., 1986. MR imaging of intravoxel incoherent motions: appli-  
564 cation to diffusion and perfusion in neurologic disorders. *Radiology* 161,  
565 401–407. doi:[10.1148/radiology.161.2.3763909](https://doi.org/10.1148/radiology.161.2.3763909).

- 566 Liang, Z.P., 2007. Spatiotemporal imaging with partially separable functions,  
567 in: 2007 4th IEEE International Symposium on Biomedical Imaging: From  
568 Nano to Macro, pp. 988–991. doi:[10.1109/ISBI.2007.357020](https://doi.org/10.1109/ISBI.2007.357020).
- 569 Liu, C., Moseley, M.E., Bammer, R., 2005. Simultaneous phase cor-  
570 rection and SENSE reconstruction for navigated multi-shot DWI with  
571 non-Cartesian  $k$ -space sampling. Magn. Reson. Med. 54, 1412–1422.  
572 doi:[10.1002/mrm.20706](https://doi.org/10.1002/mrm.20706).
- 573 Lustig, M., Donoho, D., Pauly, J.M., 2007. Sparse MRI: The application of  
574 compressed sensing for rapid MR imaging. Magn. Reson. Med. 58, 1182–  
575 1195. doi:[10.1002/mrm.21391](https://doi.org/10.1002/mrm.21391).
- 576 Mani, M., Jacob, M., Kelley, D., Magnotta, V., 2017. Multi-shot sensitivity-  
577 encoded diffusion data recovery using structured low-rank matrix comple-  
578 tion (MUSSELS). Magn. Reson. Med. 78, 494–507. doi:[10.1002/mrm.26382](https://doi.org/10.1002/mrm.26382).
- 580 Mani, M., Magnotta, V.A., Jacob, M., 2021. qModeL: A plug-and-play  
581 model-based reconstruction for highly accelerated multi-shot diffusion MRI  
582 using learned priors. Magn. Reson. Med. 86, 835–851. doi:[10.1002/mrm.28756](https://doi.org/10.1002/mrm.28756).
- 584 Mansfield, P., 1977. Multi-planar image formation using NMR spin echoes.  
585 J Phys C 10, 55–58. doi:[10.1088/0022-3719/10/3/004](https://doi.org/10.1088/0022-3719/10/3/004).
- 586 Maudsley, A.A., 1980. Multiple-line-scanning spin density imaging. J. Magn.  
587 Reson. 41, 112–126. doi:[10.1016/0022-2364\(80\)90207-3](https://doi.org/10.1016/0022-2364(80)90207-3).

- 588 Merboldt, K.D., Hanicke, W., Frahm, J., 1985. Self-diffusion NMR imaging using stimulated echoes. *J. Magn. Reson.* 64, 479–486. doi:[10.1016/0022-2364\(85\)90111-8](https://doi.org/10.1016/0022-2364(85)90111-8).
- 591 Moeller, S., Pisharady, P.K., Ramanna, S., Lenglet, C., Wu, X., Dowdle, L., Yacoub, E., Uğurbil, K., Akçakaya, M., 2021. NOise reduction with DIistribution Corrected (NORDIC) PCA in dMRI with complex-valued 593 parameter-free locally low-rank processing. *NeuroImage* 226, 117539. 594 doi:[10.1016/j.neuroimage.2020.117539](https://doi.org/10.1016/j.neuroimage.2020.117539).
- 596 Mori, S., Crain, B.J., Chacko, V.P., Van Zijl, P.C.M., 1999. Three-dimensional tracking of axonal projections in the brain by magnetic 597 resonance imaging. *Ann. Neurol.* 45, 265–269. doi:[10.1002/1531-8249\(199902\)45:2<265::AID-ANA21>3.0.CO;2-3](https://doi.org/10.1002/1531-8249(199902)45:2<265::AID-ANA21>3.0.CO;2-3).
- 600 Ong, F., Lustig, M., 2019. SigPy: A Python package for high performance 601 iterative reconstruction, in: Proceedings of the 27th Annual Meeting of 602 ISMRM, Montréal, CAN, p. 4819. doi:[10.5281/zenodo.5893788](https://doi.org/10.5281/zenodo.5893788).
- 603 Ong, F., Zhu, X., Cheng, J.Y., Johnson, K.M., Larson, P.E.Z., Vasanawala, 604 S.S., Lustig, M., 2020. Extreme MRI: Large-scale volumetric dynamic 605 imaging from continuous non-gated acquisitions. *Magn. Reson. Med.* 84, 606 1763–1780. doi:[10.1002/mrm.28235](https://doi.org/10.1002/mrm.28235).
- 607 Pipe, J.G., Farthing, V.G., Forbes, K.P., 2002. Multishot diffusion-weighted 608 FSE using PROPELLER MRI. *Magn. Reson. Med.* 47, 42–52. doi:[10.1002/mrm.10014](https://doi.org/10.1002/mrm.10014).

- 610 Polak, D., Splitthoff, D.N., Clifford, B., Lo, W.C., Huang, S.Y., Conklin, J.,  
611 Wald, L.L., Setsompop, K., Cauley, S., 2022. Scout accelerated motion  
612 estimation and reduction (SAMER). Magn. Reson. Med. 87, 163–178.  
613 doi:[10.1002/mrm.28971](https://doi.org/10.1002/mrm.28971).
- 614 Porter, D.A., Heidemann, R.M., 2009. High resolution diffusion-weighted  
615 imaging using readout-segmented echo-planar imaging, parallel imaging  
616 and a two-dimensional navigator-based reacquisition. Magn. Reson. Med.  
617 62, 468–475. doi:[10.1002/mrm.22024](https://doi.org/10.1002/mrm.22024).
- 618 Pruessmann, K.P., Weiger, M., Scheidegger, M.B., Boesiger, P., 1999.  
619 SENSE: Sensitivity encoding for fast MRI. Magn. Reson. Med. 42, 952–  
620 962. doi:[10.1002/\(SICI\)1522-2594\(199911\)42:5<952::AID-MRM16>3.0.CO;2-S](https://doi.org/10.1002/(SICI)1522-2594(199911)42:5<952::AID-MRM16>3.0.CO;2-S).
- 621
- 622 Ra, J.B., Rim, C.Y., 1993. Fast imaging using subencoding data sets from  
623 multiple detectors. Magn. Reson. Med. 30, 142–145. doi:[10.1002/mrm.1910300123](https://doi.org/10.1002/mrm.1910300123).
- 624
- 625 Roemer, P.B., Edelstein, W.A., Hayes, C.E., Souza, S.P., Mueller, O.M.,  
626 1990. The NMR phased array. Magn. Reson. Med. 16, 192–225. doi:[10.1002/mrm.1910160203](https://doi.org/10.1002/mrm.1910160203).
- 627
- 628 Setsompop, K., Fan, Q., Stockmann, J., Bilgic, B., Huang, S., Cauley, S.F.,  
629 Nummenmaa, A., Wang, F., Rathi, Y., Witzel, T., Wald, L.L., 2018. High-  
630 resolution *in vivo* diffusion imaging of the human brain with generalized  
631 slice dithered enhanced resolution: Simultaneous multislice (gSlider-SMS).  
632 Magn. Reson. Med. 79, 141–151. doi:[10.1002/mrm.26653](https://doi.org/10.1002/mrm.26653).

- 633 Setsompop, K., Gagoski, B.A., Polimeni, J.R., Witzel, T., Wedeen, V.J.,  
634 Wald, L.L., 2012. Blipped-controlled aliasing in parallel imaging for si-  
635 multaneous multislice echo planar imaging with reduced *g*-factor penalty.  
636 Magn. Reson. Med. 67, 1210–1224. doi:[10.1002/mrm.23097](https://doi.org/10.1002/mrm.23097).
- 637 Shafieizargar, B., Jeurissen, B., Poot, D.H.J., Klein, S., Van Audekerke,  
638 J., Verhoye, M., den Dekker, A.J., Sijbers, J., 2023. ADEPT: Accurate  
639 diffusion echo-planar imaging with multi-contrast shoTs. Magn. Reson.  
640 Med. 89, 396–410. doi:[10.1002/mrm.29398](https://doi.org/10.1002/mrm.29398).
- 641 Tournier, J.D., Smith, R., Raffelt, D., Tabbara, R., Dhollander, T., Pietsch,  
642 M., Christiaens, D., Jeurissen, B., Yeh, C.H., Connelly, A., 2019. MRtrix3:  
643 A fast, flexible and open software framework for medical image processing  
644 and visualisation. NeuroImage 202, 116137. doi:<https://doi.org/10.1016/j.neuroimage.2019.116137>.
- 645 Trzasko, J., Manduca, A., 2011. Local versus global low-rank promotion in  
646 dynamic MRI series reconstruction, in: Proceedings of the 19th Annual  
647 Meeting of ISMRM, Montréal, CAN, p. 4371.
- 648 Tuch, D.S., Reese, T.G., Wiegell, M.R., Makris, N., Belliveau, J.W., Wedeen,  
649 V.J., 2002. High angular resolution diffusion imaging reveals intravoxel  
650 white matter fiber heterogeneity. Magn. Reson. Med. 48, 577–582. doi:[10.1002/mrm.10268](https://doi.org/10.1002/mrm.10268).
- 651 Uecker, M., Lai, P., Murphy, M.J., Virtue, P., Elad, M., Pauly, J.M.,  
652 Vasanawala, S.S., Lustig, M., 2014. ESPIRiT – an eigenvalue approach

- 655 to autocalibrating parallel MRI: Where SENSE meets GRAPPA. Magn.  
656 Reson. Med. 71, 990–1001. doi:[10.1002/mrm.24751](https://doi.org/10.1002/mrm.24751).
- 657 Wu, W., Koopmans, P.J., Andersson, J.L., Miller, K.L., 2019. Diffusion  
658 Acceleration with Gaussian process Estimated Reconstruction (DAGER).  
659 Magn. Reson. Med. 82, 107–125. doi:[10.1002/mrm.27699](https://doi.org/10.1002/mrm.27699).
- 660 Wu, W., Miller, K.L., 2017. Image formation in diffusion MRI: A review  
661 of recent technical developments. J. Magn. Reson. Imaging 46, 646–662.  
662 doi:[10.1002/jmri.25664](https://doi.org/10.1002/jmri.25664).
- 663 Zhang, T., Pauly, J.M., Levesque, I.R., 2015. Accelerated parameter mapping  
664 with a locally low rank constraint. Magn. Reson. Med. 73, 655–661. doi:[10.1002/mrm.25161](https://doi.org/10.1002/mrm.25161).

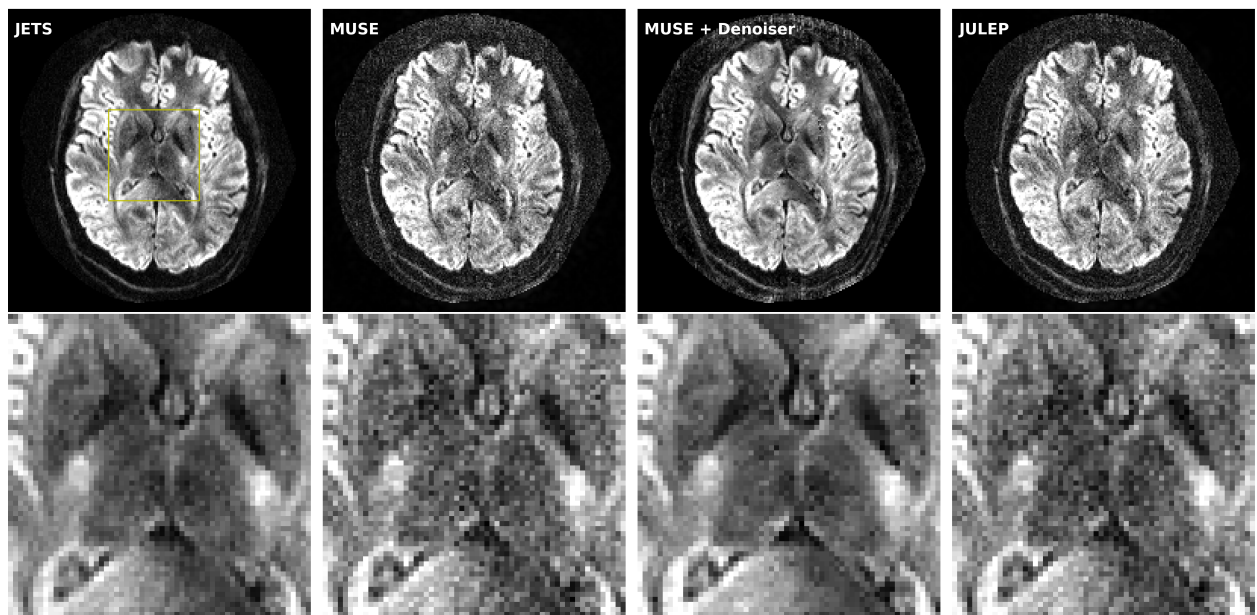
## **Supplementary Information**

### **Accelerated Diffusion Weighted Magnetic Resonance Imaging at 7 T: Joint Reconstruction for Shift-Encoded Navigator-based Interleaved Echo Planar Imaging (JETS-NAViEPI)**

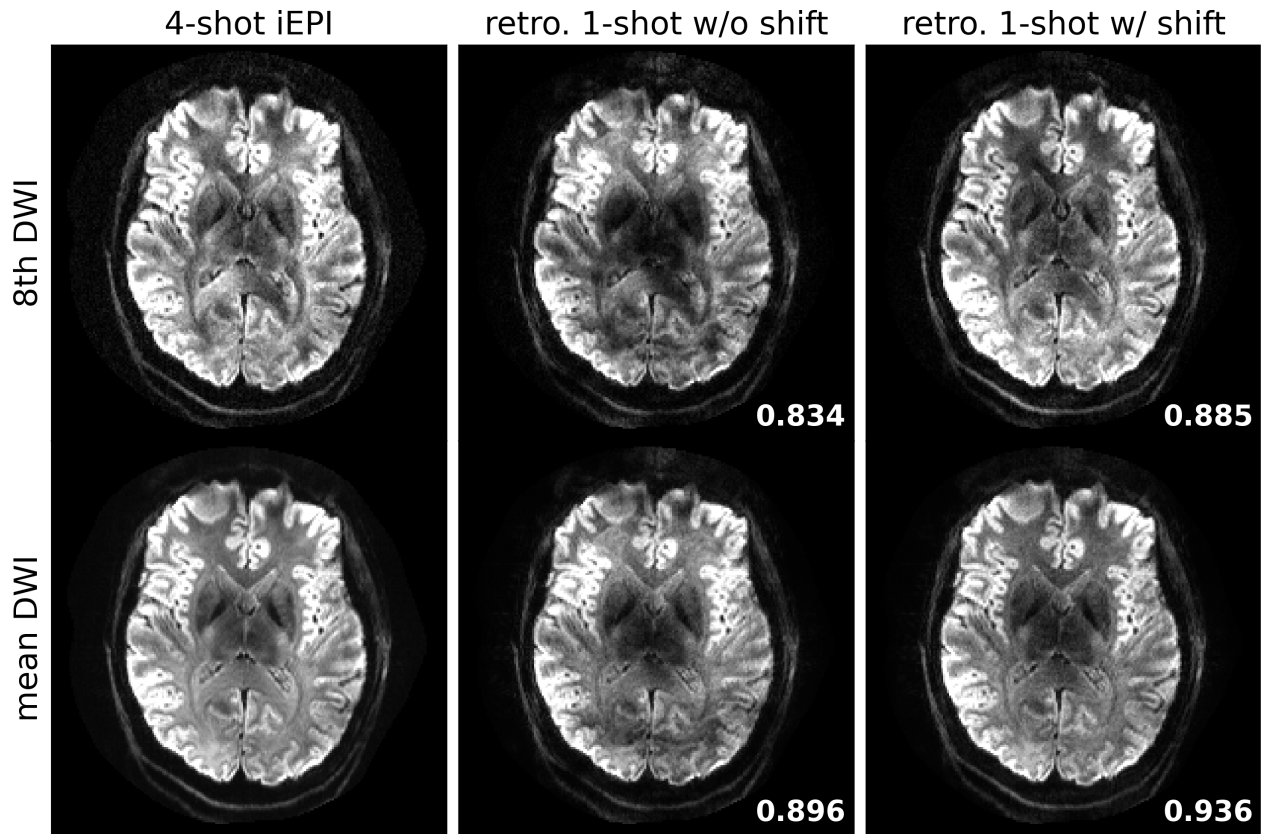
Zhengguo Tan, Patrick A. Liebig, Robin M. Heidemann, Frederik B. Laun, Florian Knoll

Here we aim to reproduce the results. Another subject with informed consent was recruited and measured by all protocols listed in Table 1 in the main manuscript.

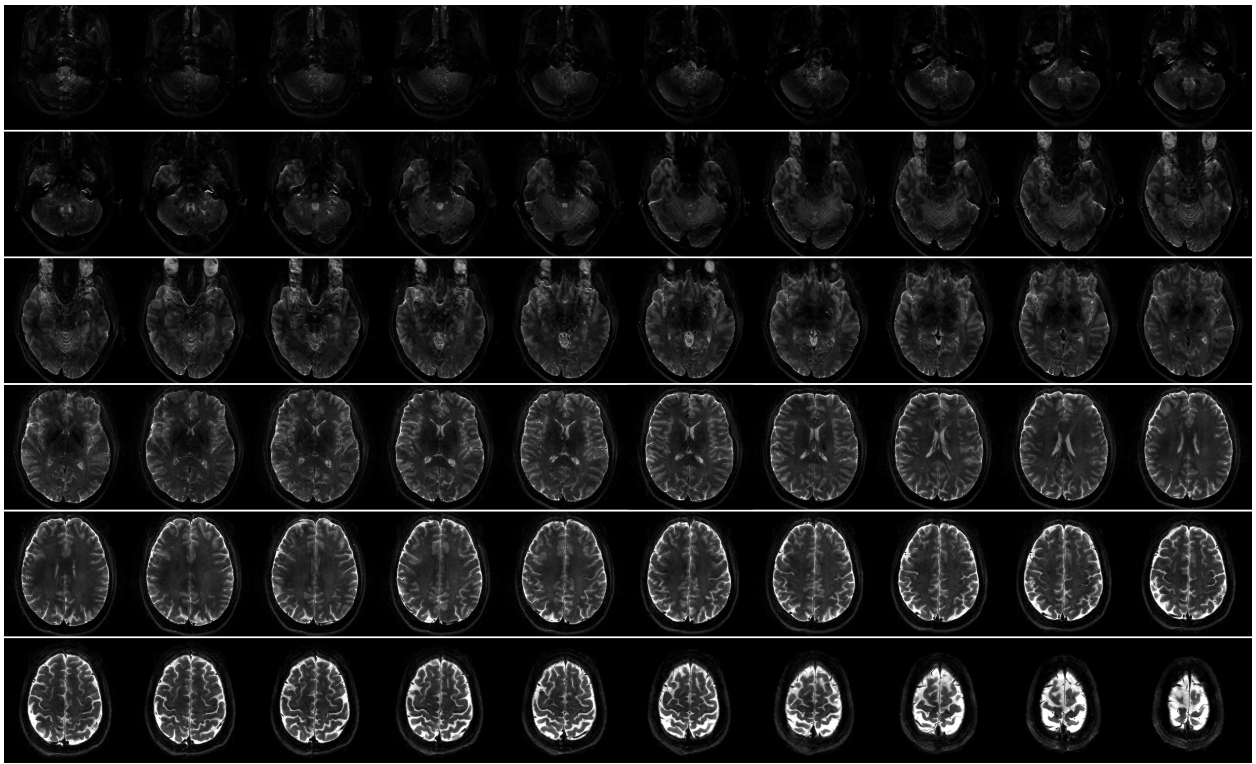
**8th DW image from 4-shot iEPI @ 1 mm ISO**



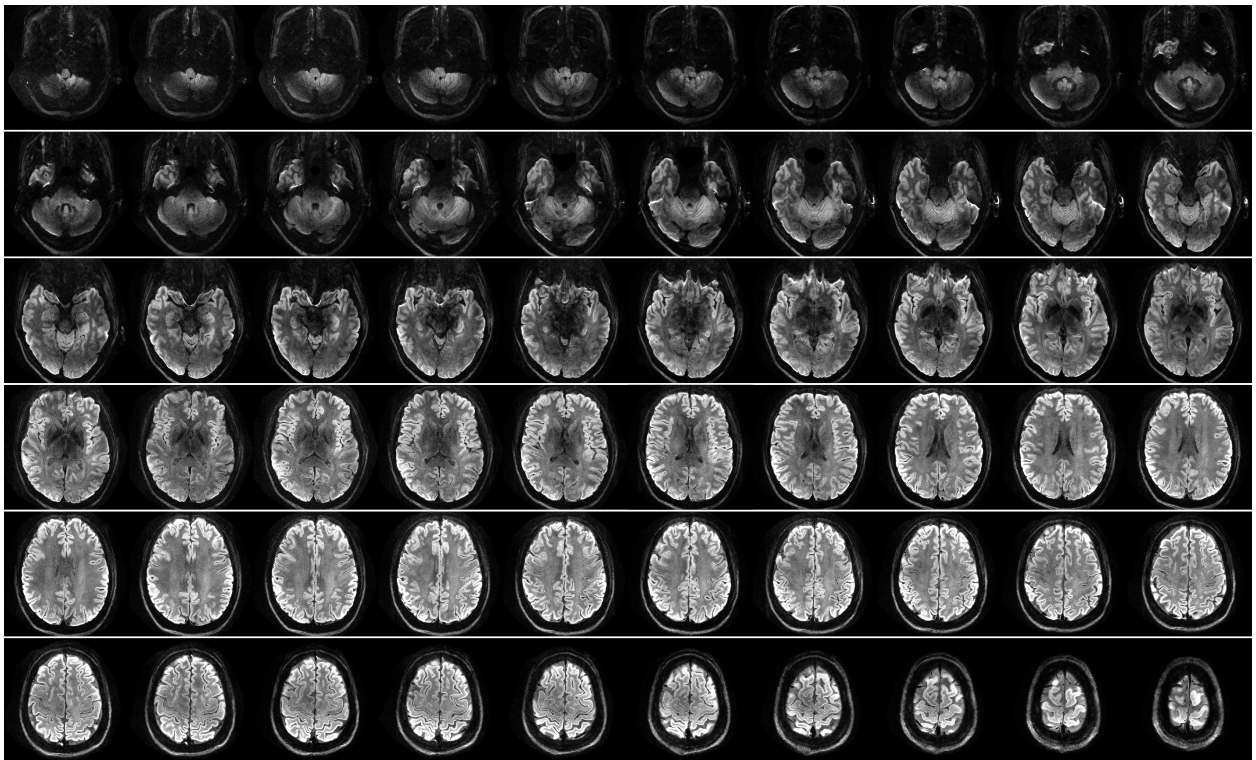
SI Figure S1: Reproducing Protocol #1. Reconstructed DW images (the 8th diffusion encoding) based on 4-shot iEPI acquisition with 1 mm isotropic resolution. Four reconstruction methods are compared (from left to right): JETS, MUSE, MUSE with denoiser, and JULEP. The 2nd row displays the magnified views of the yellow square.



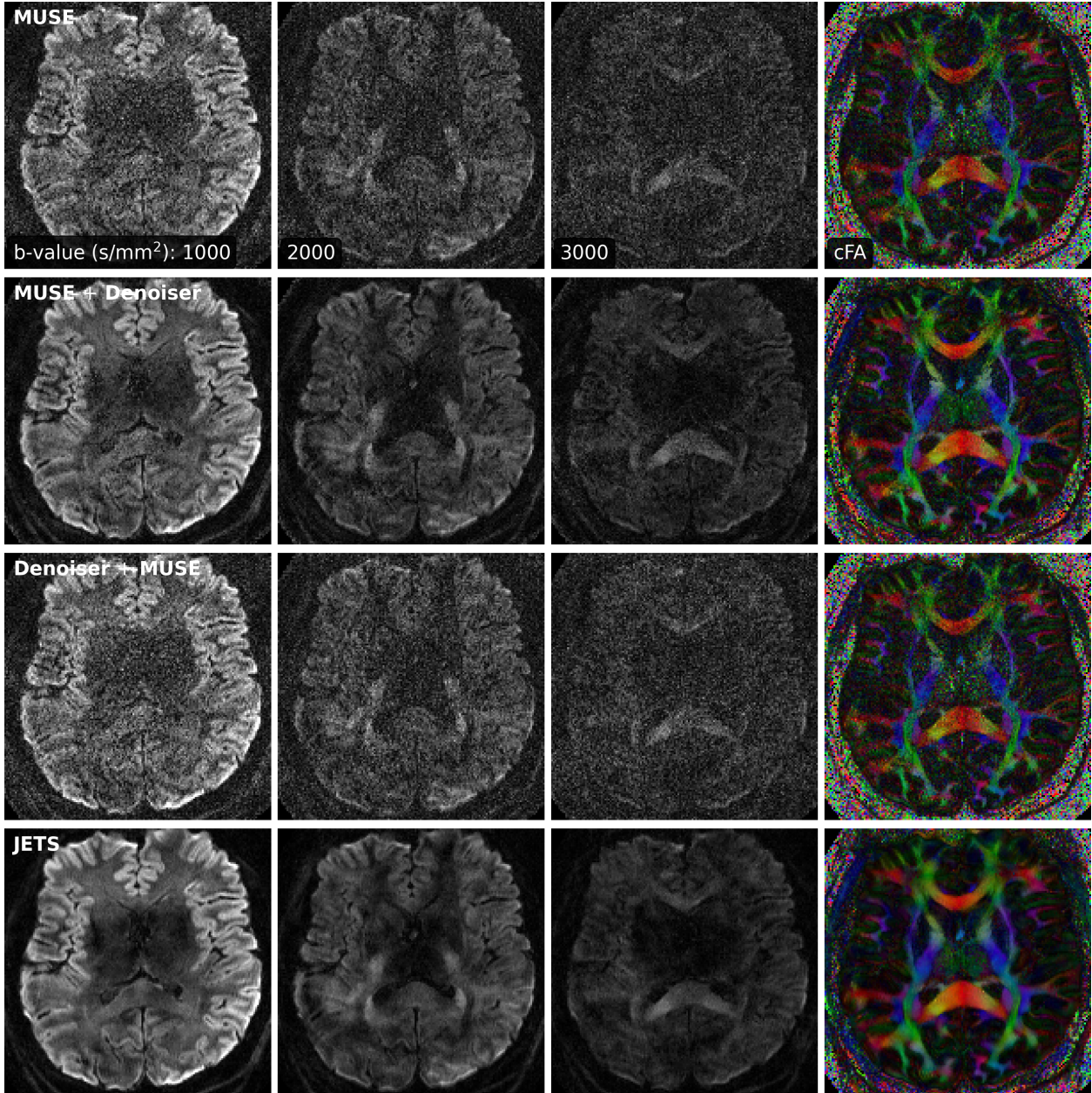
SI Figure S2: Reproducing Protocol #1. Quantitative validation of the proposed  $k_y$ -shift encoding sampling pattern based on 4-shot iEPI acquisition with 1 mm isotropic resolution. (Top) the 8th diffusion encoding and (bottom) mean DWI over 20 diffusion encodings. (1st column) JETS reconstruction of 4-shot iEPI acquisition is used as the ground truth. The 2nd and the 3rd column displays JETS reconstruction of retrospectively undersampled 1-shot acquisition without and with  $k_y$  shifting, respectively.



SI Figure S3: Reproducing Protocol #3. Reconstructed  $b_0$  images from the 3-scan trace acquisition with the voxel size  $0.5 \times 0.5 \times 2.0 \text{ mm}^3$ .



SI Figure S4: Reproducing Protocol #3. Reconstructed TRACE images from the 3-scan trace acquisition with the voxel size  $0.5 \times 0.5 \times 2.0 \text{ mm}^3$ .



SI Figure S5: Reproducing Protocol #2. The FOV and bandwidth were adapted as 200 mm and 1086 Hz/pixel, respectively. Comparison of three-shell DWIs and cFA maps reconstructed by (top to bottom) MUSE, MUSE with the local-PCA denoiser, MUSE with the local-PCA denoiser applied before the multi-shot combination, and the proposed JETS method, respectively. The local-PCA denoiser, when applied to shot images (3rd row), is less effective compared to its application to shot-combined images (2nd row). The reason is that shot images are reconstructed from the central  $k$ -space data, and thus have coarse resolution.

## **Imaging Neuroscience #203: Responses to Editors and Reviewers**

### **Editor**

Dear Zhengguo Tan,

*Thanks again for your submission. We would like to give you the opportunity to revise your paper.*

*The reviews are largely satisfied with this revision but have a few very minor points that you might consider.*

*You can access reviews and submit your revision here: <http://janeway.imaging-neuroscience.org/review/article/203/revisions/152/>*

*Your revisions are due on Jan. 12, 2024.*

*Regards,*

*Bruce Pike*

### *Imaging Neuroscience*

Thank you for the opportunity to provide another revision. We believe that this revision has further improved the quality of the manuscript and hope that it is ready for publication now.

### **Reviewer #1071**

*Authors have addressed many of my previous comments but a few pending issues persist:*

3.b.1) *Thanks for the experiment. Think I had a different implementation of MUSE reconstruction in mind when I suggested this experiment. I understand that effect would be negligible for low resolution reconstructions. I appreciate the effort but newly added result may distract from message of paper and does not add much. Therefore, I'd remove it.*

Thank you for the suggestion. We feel this additional experiment that you suggested in a previous revision round adds value to the manuscript and we chose to keep it.

3.b.2) *I don't think that current discussion is focusing on synergies rather than on similarities. This might be fine, but I suggest to rephrase to provide opinion on whether these methods could complement each other or not.*

Thank you for the specific suggestion. We rewrote this paragraph. Please refer to the highlighted manuscript with the note R1071.3.b.2.

4.a) *Caption Fig. 6b: "varying block width, keeping lambda 0.08 and stride 1" → "varying block width, keeping lambda as 0.08 and stride as 1"*

Done.

7) L336: "Figs. 6 and 7 select" → "Figs. 6 and 7 show"

L338: "the lower brain region which identifies the" → "an inferior brain region with marked"

L339: "the middle" → "a middle" L440: "the upper brain" → "a superior brain"

Done.

9) Thanks for testing the normalization. Seems it is an appropriate prevention for differentiating lambda levels and block size effects. In my opinion authors should replace current Fig. 6 with normalized counterpart, identify new optimal set of parameters, incorporate normalization to manuscript methods, and rerun paper experiments with new optimal configuration.

Thank you for the suggestion. We included the normalization strategy in the manuscript.

12) L270-271: "and even partially removes phase variation" → "and partially removes phase variation"

Done.